University of Windsor

Scholarship at UWindsor

Electronic Theses and Dissertations

Theses, Dissertations, and Major Papers

2008

Flammable mixture formation in a transient gaseous fuel injection process

Nima Gharib

University of Windsor

Recommended Citation

Gharib, Nima, "Flammable mixture formation in a transient gaseous fuel injection process" (2008). *Electronic Theses and Dissertations*. 7916.
https://scholar.uwindsor.ca/etd/7916

Vita Auctoris

Name:	Nima Gharib
Place of birth:	Tehran, Iran
Year of Birth:	1982
Education:	Daneshmand High School, Iran, Tehran 1997-2000
	University of Tehran, Iran, Tehran 2001-2005 B.Sc.
	University of Windsor, Ontario, Windsor 2006-2008 M.Sc.

Flammable Mixture Formation in a Transient Gaseous Fuel Injection Process

by

Nima Gharib

A Thesis
Submitted to the Faculty of Graduate Studies
through the Department of Mechanical, Automotive, and Materials Engineering
in Partial Fulfillment of the Requirements for
the Degree of Master of Applied Science at the
University of Windsor

Windsor, Ontario, Canada
2008

Library and
Archives Canada

Published Heritage
Branch

395 Wellington Street
Ottawa ON K1A 0N4
Canada

Bibliothèque et
Archives Canada

Direction du
Patrimoine de l'édition

395, rue Wellington
Ottawa ON K1A 0N4
Canada

Your file Votre référence
ISBN: 978-0-494-47083-1
Our file Notre référence
ISBN: 978-0-494-47083-1

NOTICE:
The author has granted a non-exclusive license allowing Library and Archives Canada to reproduce, publish, archive, preserve, conserve, communicate to the public by telecommunication or on the Internet, loan, distribute and sell theses worldwide, for commercial or non-commercial purposes, in microform, paper, electronic and/or any other formats.

The author retains copyright ownership and moral rights in this thesis. Neither the thesis nor substantial extracts from it may be printed or otherwise reproduced without the author's permission.

AVIS:
L'auteur a accordé une licence non exclusive permettant à la Bibliothèque et Archives Canada de reproduire, publier, archiver, sauvegarder, conserver, transmettre au public par télécommunication ou par l'Internet, prêter, distribuer et vendre des thèses partout dans le monde, à des fins commerciales ou autres, sur support microforme, papier, électronique et/ou autres formats.

L'auteur conserve la propriété du droit d'auteur et des droits moraux qui protège cette thèse. Ni la thèse ni des extraits substantiels de celle-ci ne doivent être imprimés ou autrement reproduits sans son autorisation.

In compliance with the Canadian Privacy Act some supporting forms may have been removed from this thesis.

While these forms may be included in the document page count, their removal does not represent any loss of content from the thesis.

Conformément à la loi canadienne sur la protection de la vie privée, quelques formulaires secondaires ont été enlevés de cette thèse.

Bien que ces formulaires aient inclus dans la pagination, il n'y aura aucun contenu manquant.

Canada

Authors Declaration of Originality

I hereby certify that I am the sole author of this thesis and that no part of this thesis has been published or submitted for publication.

I certify that, to the best of my knowledge, my thesis does not infringe upon anyones copyright nor violate any proprietary rights and that any ideas, techniques, quotations, or any other material from the work of other people included in my thesis, published or otherwise, are fully acknowledged in accordance with the standard referencing practices. Furthermore, to the extent that I have included copyrighted material that surpasses the bounds of fair dealing within the meaning of the Canada Copyright Act, I certify that I have obtained a written permission from the copyright owner(s) to include such material(s) in my thesis and have included copies of such copyright clearances to my appendix.

I declare that this is a true copy of my thesis, including any final revisions, as approved by my thesis committee and the Graduate Studies office, and that this thesis has not been submitted for a higher degree to any other University or Institution.

Abstract

In this study the effects of angular momentum (tumble and swirl) on flammable mixture formation between chamber air and transient gaseous jets of hydrogen and methane have been numerically investigated in fixed volume cubic and cylindrical chambers, and in a variable volume cylindrical chamber with moving piston. The magnitude of the angular momentum, injection duration, and injection velocity are the main parameters whose effects have been studied on flammable mixture formation and mixing rate. The numerical simulations were carried out with the use of KIVA3V. the code is modified for gaseous injection with standard $k-\epsilon$ model for turbulence. It was found that hydrogen and air mixing, under application of angular momentum, leads to faster formation of flammable mixture, with mixing rates several times larger than those of methane. Also dynamics of the hydrogen mixing is markedly different from that for methane with the same magnitude of angular momentum. Dissipation of bulk vortex, and angular momentum decay during compression were also studied. The results for the cylinder with moving piston show the disappearance of tumbling motion at the end of compression while the swirling motion is preserved until the expansion stroke.

Acknowledgement

I would like to acknowledge the support of my advisor Prof. Andrezj Sobiesiak throughout this effort. His insightful scientific suggestions helped me avoid research avenues that would lead me to inappropriate and fruitless conclusions. His friendship eased my mind at times when problems with research were overwhelming my thoughts.

I would like to thank my committee members, Dr. R. Barron, Dr. G. Rankin, and Dr. N. Zamani, whose valuable comments improved the contents of this thesis.

Finally, I would like to thank my friends Michael Johnson, Srikanth Jonnalagedda, Clarence Mulenga, Prakash Gnanam, Dale Haggith, Hamid Totonchian, and Mohsen Battoie for their support.

Contents

Appendix

List of Tables

List of Figures

Nomenclature

A_{inj} : Injector nozzle exit area

ASR : Arbitrary swirl ratio

ATR : Arbitrary tumble ratio

c_p : Specific heat at constant pressure

$c_\mu, c_{\epsilon_1}, c_{\epsilon_2}, c_{\epsilon_3}$: Constants in standard $k-\epsilon$ model

D : Injector nozzle exit diameter

$\mathbf{g}$: Gravity vector

h : Enthalpy

I : Internal energy

$\mathbf{i}, \mathbf{j}, \mathbf{k}$: Principal unit vectors in x, y, z directions

$\mathbf{J}$: Heat flux vector

K : Conductivity

k : Turbulent kinetic energy

m : Mass

$\dot{m}$: Mass flow rate

P : Pressure

Pr_k,Pr_ϵ : Constants in standard $k-\epsilon$ model

Re : Reynolds number

R_0 : Universal gas constant

SR : Swirl ratio

T : Temperature

t : Time

t_{inj} : Injection time

t_{sinj} : Start of injection

TDC : Top dead center

TR : Tumble ratio

$\mathbf{u}$: Velocity vector

u, v, w : Velocity components in x, y, z directions

W : Molecular weight

$\mathbf{x}$: Position vector

Greek Symbols

δ : Derivative operator

ϵ : Dissipation rate

μ : Dynamic viscosity of fluid

ν : Kinematic viscosity of fluid

ρ : Density

σ : Viscosity tensor

∇ : Gradient operator

Subscripts

a : Ambient (chamber)

inj : Injection

m : Relative to species

rms : Root mean square

$stoic$: Stoichiometric

Chapter 1

Introduction

Different types of engine are shown in Figure 1.1. In compression ignition engines, air is provided during the intake stroke and it undergoes compression. During compression the temperature and pressure of air increase. Near top dead center the fuel is sprayed into the chamber and combustion occurs between injected fuel and compressed air. The fuel and air are separated by flame front and combustion products. In spark ignition engine, fuel and air was mixed before the intake stroke. The mixture is ignited by the use of spark plug slightly before top dead center. Auto ignition of the mixture limits the compression ratio in spark ignition engines. The third type of engines, which is believed to be used in the next generation of internal combustion engines are homogenous charge compression ignition engines (HCCI). In HCCI engines mixture of fuel and air is provided into the cylinder and combustion occurs without the need of spark plug. The combustion phenomena almost happen everywhere in the cylinder at the same time. Thus, the heat transfer process is faster and approaches constant volume. This will increase the efficiency and improve the fuel economy.

Simultaneous combustion of air and fuel in HCCI engines and mechanical and thermal properties of materials restrict the equivalence ratio of the charge. On the other hand, in HCCI engines very lean mixture should be brought into the cylinder. Lean mixtures are hard to ignite. There are several approaches increasing the ignition possibilities of lean mixtures. Increasing their temperature or pressure before intake stroke or during compression stroke is one approach which is limited by thermal and mechanical stresses. Enhancing turbulent intensity in side the cylinder is another way recently found its way in internal combustion engine researcher studies. High level of turbulence inside the cylinder produce more effective flame front speed and permits ignition of lean mixture, more exhaust gas recirculation (EGR).

Providing bulk motion of air inside the cylinder by different means are employed by car manufactures to increase turbulent characteristics inside the cylinder. The bulk motion of air can be generated during intake stroke by shaping intake manifold to create desire motion or using different type of shrouded valve or changing the design of piston crown so that during compression it creates bulk motion of air.

The lack of

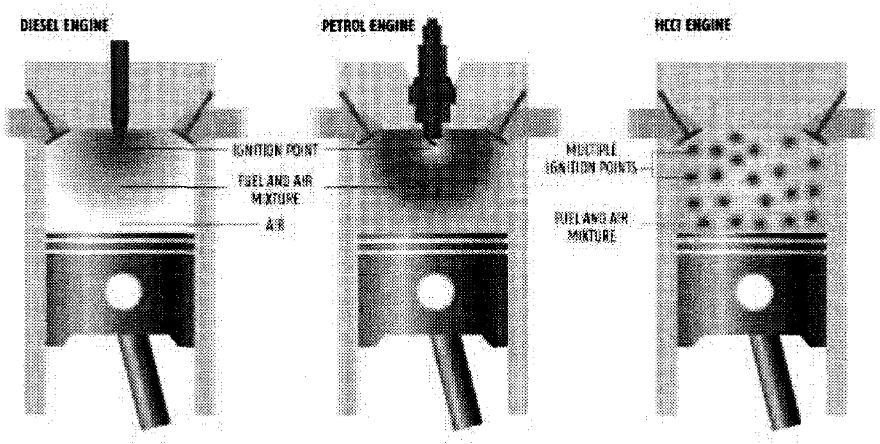

Fig. 1.1: Diesel, spark ignition, and HCCI engines (ww.me.berkeley.edu)

1.1 Transient Jets

As the injector is actuated, a gaseous jet is injected though the nozzles and propagates across the combustion chamber. Photographic evidence of impulsively started jets shows that a vortex head is formed and propagates away from the nozzle [3, 4], as depicted schematically in Figure 1.2. In a so-called puff jet, the vortex head contains all of the injected fluid. In a transient jet, a quasi-steady jet is formed behind the vortex head. Flow visualization of the transient jet indicates that, for engine application, the jets are of the latter type [5].

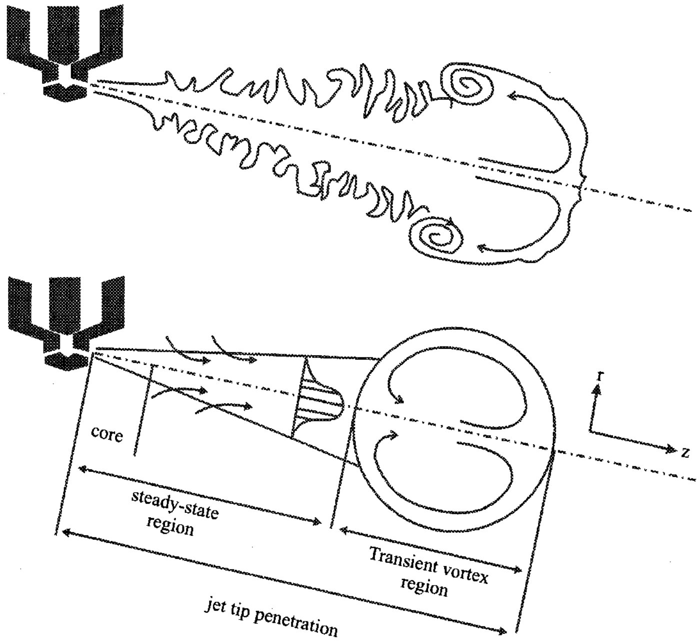

Fig. 1.2: Turbulent transient jet structure and model [1].

When the maximum Mach number in the jet is below approximately 0.3, compressibility effects are negligible. Incompressible steady-state jets have been widely studied [2, 6, 7]. Behind the vortex head, the jet is considered steady. The steady part of the jet feeds mass and momentum to the vortex head, causing its mass, momentum and size to increase. The vortex head travels according to its own momentum, being slowed down by frictional forces and by the need to accelerate the surrounding fluid.

As one fluid is injected at a certain velocity into another fluid whose pressure field is uniform, a mixing layer develops between the injected fluid and surrounding gas. Mass from the surrounding gas is entrained in the injected fluid. For incompressible air jets issuing from round nozzles into stagnant air, the rate of entrainment is found to be proportional to the distance from the nozzle and to the mass injection rate. The mass flow rate $\dot{m}$ at a cross-section of the jet is given by,

$$\frac{\dot{m}}{\dot{m}_n} = 0.32\frac{z}{d_n} \tag{1.1}$$

where $\dot{m}_n$ is the mass flow rate at the nozzle, z is the distance from the nozzle and d_n is the nozzle diameter. This relationship was verified experimentally by direct measurement of the mass entrainment rate, from which the constant of 0.32 was obtained. The mass entrainment rate was found to be independent of the nozzle Reynolds number if Re isgreater than 2×10^4 [1].

The turbulent steady-state jet can be divided into three regions: a central core, a transition region, and a fully developed region. In the central core, there is a region where the velocity is uniform because the mixing has not taken place yet. In the fully developed region, the velocity profile is said to be self-similar. Similarity is a well-observed feature of turbulent jets, and indicates that non-dimensional velocity profiles are independent of the distance from the nozzle,

$$\frac{U(r,z)}{U_{cl}(z)} = f(\eta) \qquad \eta = \frac{r}{R} \tag{1.2}$$

where $U(r,z)$ is the velocity at a distance z from the nozzle and at a normal distance r from the jet axis, U_{cl} is the center line velocity at z, and R is the radial extent of the jet at z. The jet front is defined where the mass fraction is about 5%. Typically the fully developed region starts at a distance of 10 to 20 diameters from the nozzle.

1.2 Objectives

Since the direct injection gas technology is new, minimal understanding of the direct injection gas mixing process is currently exists. Such understanding need is needed to help guide the continued development required to reduce emissions to meet future emissions standards, and improve combustion stability. Such understanding should also lead to development of analytical models that would be used to facilitate technology transfer to other engines and applications. Therefore, some key questions remain regarding the fuel/air mixing processes in the cylinder. These include the following:

How does combustion chamber design affect mixing? What are the gaseous fuel and air mixing rates, and how can it be optimized? What is the fuel/air ratio distribution in the chamber and how it can be improved? How will mixing characteristics varies for hydrogen and natural gas? What would be the effect of bringing bulk motion of air in the chamber on mixing process? How will the bulk motion of air decay with the movement of piston?

1.3 Methodology

Standard tool for performing 3D CFD computations (KIVA3V) is used to model transient gaseous fuel jet into fixed and variable volumes. Cubic and cylindrical geometries because of having simple geometry and their application as combustion chamber in gas turbines and internal combustion engines were chosen as the fixed volumes. Gaseous fuel were injected only in cylindrical chamber with moving piston as the variable volume chamber. Before the injection, velocity profile of air inside the chambers was set using Bessel function. This bulk motion of air can have axis of rotation parallel or normal to the axis of piston. For each case different and for six different angular momentum, hydrogen and methane were injected and the mixture formation and mixing rate over the time were studied. The behavior of bulk vortex with the movement of piston were also considered.

Chapter 2

Literature Review

There has been much work done on direct injection of transient gaseous jets [6, 8–11]. The penetration depth and the entrainment rate of these types of jets are documented in several references [2, 12]. However, there are only a few studies on the mixture preparation of transient gaseous fuel jet in bulk motion of air [13, 14].

Gaseous fuel jet can be injected directly into the combustion chamber with high pressure or into the intake port before intake stoke. In the first case the flow is supersonic and the Mach number at the nozzle exit is unity, in the later case the flow is considered incompressible and mass flow rate depends on the injection pressure.

Hill and Ouellette [12] studied the effects of parameters such as injection pressure, number of nozzles, and temperature and pressure of the air inside the chamber on mixture formation. Their work was mainly focused on high pressure injection of natural gas. Natural gas, because of its low flame temperature, offers a potential for reduced NO_x (nitrogen oxide). Also owing to the simpler chemical structure of methane, which constitutes 90 to 98 % of natural gas, the potential to form particulate matter and unburned hydrocarbons during combustion is reduced. In Hill and Ouellette [12]'s work, injection pressure is higher than the critical pressure (1.83 for methane, assuming ideal gas behavior), the pressure at the exit nozzle plane is greater than chamber pressure, and under-expansion occurs outside the nozzle. Under-expansion is a complex adjustment process involving expansion waves and compression waves which form a barrel shaped shock pattern. Figure 2.1 shows the process of the expansion outside the nozzle. Comparison of mixing rates using different number of nozzles with equal momentum injection rate and equal mass injection rate are shown in Figure 2.2. The results confirm that using more nozzles of smaller diameter increases the mixing between the fuel and the chamber air [12]. The results can also be understood by considering that the total volume of rich cores is smaller for smaller nozzles than for larger ones. The formation rate of flammable fuel fraction is very similar for both cases. In this study, the flammable mixture volume over time is modeled, so the number of nozzles was not taken into account. However, our results for two nozzles with the same total nozzle exit area confirm Ouellette [1]'s conclusions that the volume of the combustible region remains the same during injection time.

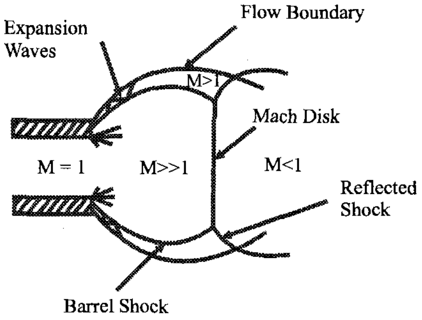

Fig. 2.1: Schematic of under-expansion process.

Xia [2] measured penetration depth of different gaseous fuel jets being injected into the semi-homogenous turbulent field created in a cubic chamber. A pair of perforated plates were employed to generate a homogenous turbulent field in the middle part of the cube where the measurements were made. Hole diameters, oscillating frequency, and stroke are the parameters by which the desired turbulent kinetic energy and turbulent length scale were adjusted. Figure 2.3 shows the flammable mass fraction of methane. The cases with '20 Hz, stopped while injecting produces a little faster increase of mass fraction of mixed methane than the jet injected into quiescent chamber

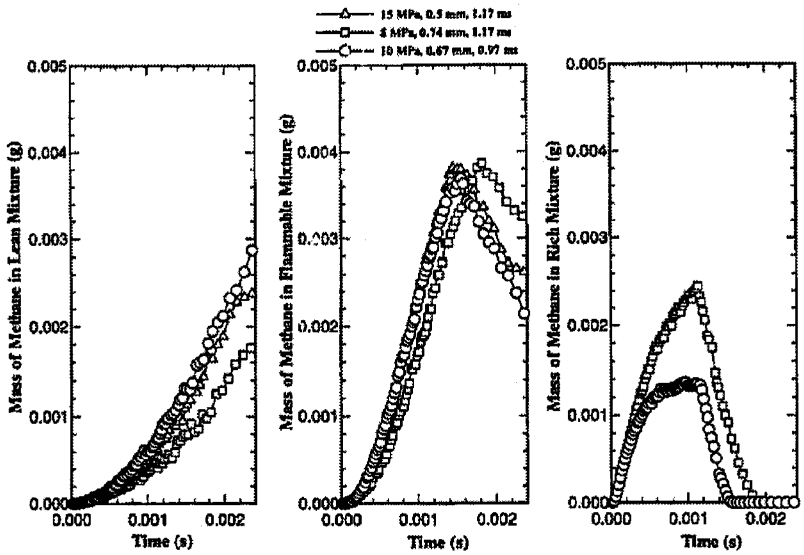

Fig. 2.2: Mixing rate for cases with equal momentum injection rate and equal mass injection rate [1].

air.

Measured data of penetration depth of methane are shown in Figure 2.4. Linear dependency between penetration depth and square root of time are clearly depicted.

Tsujimura et al. [15] studied development and combustion characteristics of hydrogen jets in a constant volume vessel. The effects of injection duration, pressure and orifice diameter on the discharge coefficient and mass flow rate were examined, and the following observation can be made:

- When the injection pressure is about twice of the ambient gas pressure, the discharge coefficient is approximately constant and the mass flow rate increases in proportion to the injection pressure.

- The orifice diameter has no effect on the discharge coefficient, and the mass flow rate depends linearly on the cross section area of the orifice.

- The injection pressure has a weak effect on the jet penetration, dispersion angle, and average equivalence ratio under the experimental conditions.

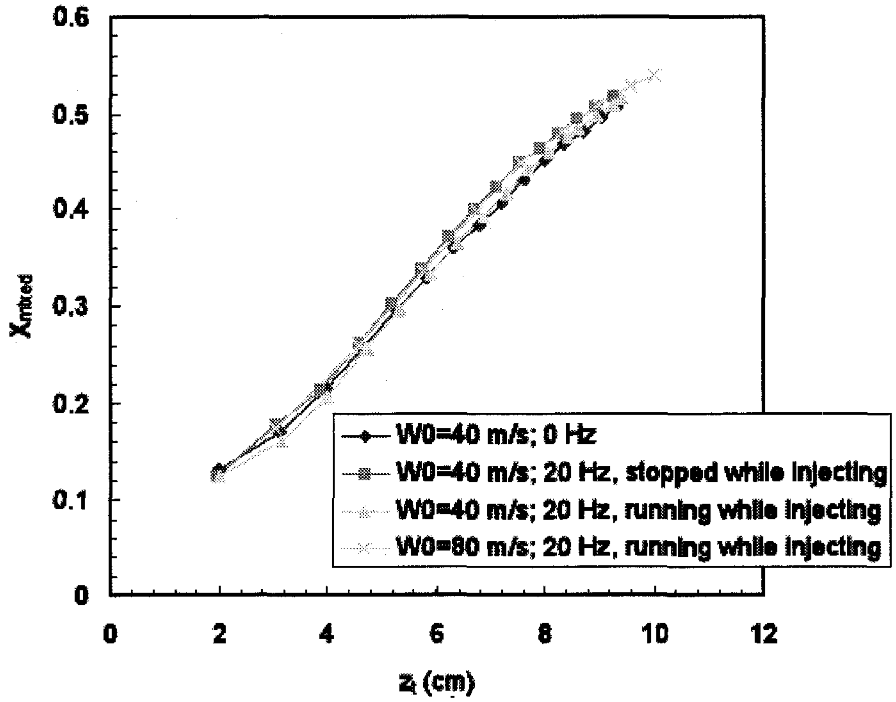

Fig. 2.3: Changes of percentage of flammable methane with penetration depth.[2].

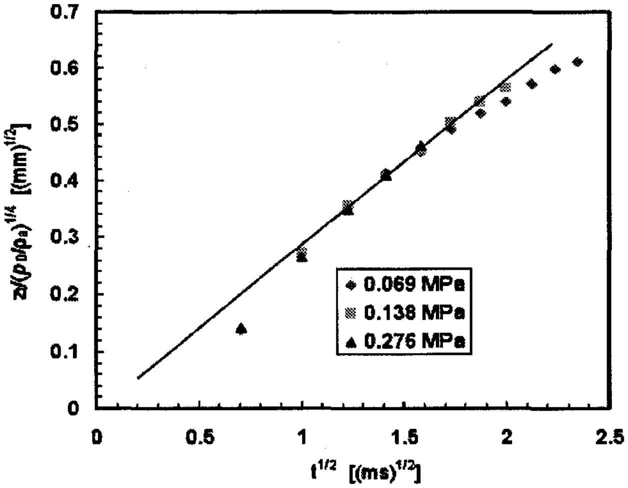

Fig. 2.4: Penetration depth vs. square root of time [2].

- Under relatively higher ambient gas density conditions, the hydrogen jet is incapable of developing in the axial direction. But the jet can entrain a great amount of the ambient gas, causing the significant decrease in the average equivalence ratio of the jet.

- As the hydrogen jet is injected through a smaller orifice, the average equivalence ratio in the jet significantly decreases.

Tomita et al. [7] used a CCD camera to measure spatial and temporal changes of air entrainment into the hydrogen jet. Hydrogen was injected through an electromagnetically controlled injector, which is widely used for the injection of gasoline into the intake port in spark-ignition engines. The results show that total air mass entrained into the flame jet is nearly equal to that into the cold jet. The rate of entrainment per unit area of the flame is smaller than that in the cold jet. When a transient jet is separated into side and front parts, the rate of air mass entrained from the front part of the jet decreases with time while the rate into the side of the jet per unit area is almost the same.

Schlieren method and Rayleigh scattering were used by Koyanagi et al. [16] to visualize mixture formation of hydrogen and measure local concentration of hydrogen. The mixture formation was also studied by Kaiser and White [17] using acetone Planar Laser-Induced Fluorescence (PLIF) and Particle Image Velocimetry (PIV) in a single-cylinder engine fueled with hydrogen.

Studies on the effect of bulk motion of air on mixture formation are limited to internal combustion engines with liquid fuel spray. Stansfield et al. [18] investigated the in-cylinder flow structure DI gasoline engine over realistic engine speeds using PIV analysis. Tumbling and Swirling motion created in a four-valve SI engine using different shapes of the intake valves were studied by Baumgarten et al. [9] and Li et al. [14]. Hong and Trang [19] and Shuliang et al. [13] employed Laser Doppler Velocimetry (LDV) to determine tumble flow field in SI engine.

Chapter 3

Simulation in KIVA

In order to analyze the effects of bulk motion of air, injection velocity, injection time, and chamber geometry, two simulation matrices were set up as listed in Table 3.1 and Table 3.2 for methane and hydrogen, respectively. The variable parameters are: a) the chamber geometry, fixed volume chambers (cubic or cylindrical) or variable volume chamber (cylindrical chamber with moving piston), b) the magnitude and direction of the bulk motion of air, (swirl with axis of rotation parallel to axis of piston, and tumble with axis of rotation normal to the axis of piston). Five levels of tumbling and swirling motion were imposed during the simulations. The ratio of angular velocity of the bulk motion of air to that of the engine is called swirl ratio (SR), or tumble ratio (TR) depending on their axis of rotation. In the case of fixed volume, an arbitrary swirl ratio (ASR) and an arbitrary tumble ratio (ATR) were defined in which the angular velocity corresponds to an engine with *rpm* of 2400. Other parameters are c) injection velocity, u_{inj} and, d) injection time, t_{inj}. These two quantities are related to each other, their values are selected based on intake port injection and the assumption that if the mixture is perfectly mixed the equivalence ratio lies between $\phi \approx 0.8-0.9$. The final parameter is e) start of injection t_{sinj}, which sets the beginning of gaseous injection in the code and is used only for the variable volume chamber with moving piston. Two sets of data are obtained for the cylindrical chamber with moving piston. In the first case, injection starts from $t_{sinj} = 0.0$ and in the second case injection starts when the piston goes half way up to the top dead center (TDC), $t_{sinj} = 6.25\,(ms)$. Methane and hydrogen we selected as the gaseous fuel jet because of their simple chemical structure and their low flame temperature the y have potential to reduce emissions. The values of injection time and injection velocity were selected based on intake port injection.

Overall 88 cases (44 hydrogen injection, 44 methane injection) were simulated in this study.

Table 3.1: Simulation matrix - CH_4

Case	Chamber	SR	TR	$u_{inj}(m/s)$	$t_{sinj}(ms)$	$t_{inj}(ms)$
$CH_4 - 1$	Cubic	0.0	0.0	150	0.0	10.0
$CH_4 - 2$	Cubic	0.5	0.0	150	0.0	10.0
$CH_4 - 3$	Cubic	1.0	0.0	150	0.0	10.0
$CH_4 - 4$	Cubic	1.5	0.0	150	0.0	10.0
$CH_4 - 5$	Cubic	2.0	0.0	150	0.0	10.0
$CH_4 - 6$	Cubic	2.5	0.0	150	0.0	10.0
$CH_4 - 7$	Cubic	0.0	0.5	150	0.0	10.0
$CH_4 - 8$	Cubic	0.0	1.0	150	0.0	10.0
$CH_4 - 9$	Cubic	0.0	1.5	150	0.0	10.0
$CH_4 - 10$	Cubic	0.0	2.0	150	0.0	10.0
$CH_4 - 11$	Cubic	0.0	2.5	150	0.0	10.0
$CH_4 - 12$	Cylindrical	0.0	0.0	150	0.0	10.0
$CH_4 - 13$	Cylindrical	0.5	0.0	150	0.0	10.0
$CH_4 - 14$	Cylindrical	1.0	0.0	150	0.0	10.0
$CH_4 - 15$	Cylindrical	1.5	0.0	150	0.0	10.0
$CH_4 - 16$	Cylindrical	2.0	0.0	150	0.0	10.0
$CH_4 - 17$	Cylindrical	2.5	0.0	150	0.0	10.0
$CH_4 - 18$	Cylindrical	0.0	0.5	150	0.0	10.0
$CH_4 - 19$	Cylindrical	0.0	1.0	150	0.0	10.0
$CH_4 - 20$	Cylindrical	0.0	1.5	150	0.0	10.0
$CH_4 - 21$	Cylindrical	0.0	2.0	150	0.0	10.0
$CH_4 - 22$	Cylindrical	0.0	2.5	150	0.0	10.0
$CH_4 - 23$	Cylindrical - moving	0.0	0.0	150	0.0	10.0
$CH_4 - 24$	Cylindrical - moving	0.5	0.0	150	0.0	10.0
$CH_4 - 25$	Cylindrical - moving	1.0	0.0	150	0.0	10.0
$CH_4 - 26$	Cylindrical - moving	1.5	0.0	150	0.0	10.0
$CH_4 - 27$	Cylindrical - moving	2.0	0.0	150	0.0	10.0
$CH_4 - 28$	Cylindrical - moving	2.5	0.0	150	0.0	10.0
$CH_4 - 29$	Cylindrical - moving	0.0	0.5	150	0.0	10.0
$CH_4 - 30$	Cylindrical - moving	0.0	1.0	150	0.0	10.0
$CH_4 - 31$	Cylindrical - moving	0.0	1.5	150	0.0	10.0
$CH_4 - 32$	Cylindrical - moving	0.0	2.0	150	0.0	10.0
$CH_4 - 33$	Cylindrical - moving	0.0	2.5	150	0.0	10.0

Table 3.1 Simulation matrix - CH_4 cont.

Case	Chamber	SR	TR	$u_{inj}(m/s)$	$t_{sinj}(ms)$	$t_{inj}(ms)$
$CH_4 - 34$	Cylindrical - moving	0.0	0.0	300	6.25	5.0
$CH_4 - 35$	Cylindrical - moving	0.5	0.0	300	6.25	5.0
$CH_4 - 36$	Cylindrical - moving	1.0	0.0	300	6.25	5.0
$CH_4 - 37$	Cylindrical - moving	1.5	0.0	300	6.25	5.0
$CH_4 - 38$	Cylindrical - moving	2.0	0.0	300	6.25	5.0
$CH_4 - 39$	Cylindrical - moving	2.5	0.0	300	6.25	5.0
$CH_4 - 40$	Cylindrical - moving	0.0	0.5	300	6.25	5.0
$CH_4 - 41$	Cylindrical - moving	0.0	1.0	300	6.25	5.0
$CH_4 - 42$	Cylindrical - moving	0.0	1.5	300	6.25	5.0
$CH_4 - 43$	Cylindrical - moving	0.0	2.0	300	6.25	5.0
$CH_4 - 44$	Cylindrical - moving	0.0	2.5	300	6.25	5.0

Table 3.2: Simulation matrix - H_2

Case	Chamber	SR	TR	$u_{inj}(m/s)$	$t_{sinj}(ms)$	$t_{inj}(ms)$
$H_2 - 1$	Cubic	0.0	0.0	150	0.0	20.0
$H_2 - 2$	Cubic	0.5	0.0	150	0.0	20.0
$H_2 - 3$	Cubic	1.0	0.0	150	0.0	20.0
$H_2 - 4$	Cubic	1.5	0.0	150	0.0	20.0
$H_2 - 5$	Cubic	2.0	0.0	150	0.0	20.0
$H_2 - 6$	Cubic	2.5	0.0	150	0.0	20.0
$H_2 - 7$	Cubic	0.0	0.5	150	0.0	20.0
$H_2 - 8$	Cubic	0.0	1.0	150	0.0	20.0
$H_2 - 9$	Cubic	0.0	1.5	150	0.0	20.0
$H_2 - 10$	Cubic	0.0	2.0	150	0.0	20.0
$H_2 - 11$	Cubic	0.0	2.5	150	0.0	20.0
$H_2 - 12$	Cylindrical	0.0	0.0	150	0.0	20.0
$H_2 - 13$	Cylindrical	0.5	0.0	150	0.0	20.0
$H_2 - 14$	Cylindrical	1.0	0.0	150	0.0	20.0
$H_2 - 15$	Cylindrical	1.5	0.0	150	0.0	20.0
$H_2 - 16$	Cylindrical	2.0	0.0	150	0.0	20.0
$H_2 - 17$	Cylindrical	2.5	0.0	150	0.0	20.0
$H_2 - 18$	Cylindrical	0.0	0.5	150	0.0	20.0
$H_2 - 19$	Cylindrical	0.0	1.0	150	0.0	20.0
$H_2 - 20$	Cylindrical	0.0	1.5	150	0.0	20.0
$H_2 - 21$	Cylindrical	0.0	2.0	150	0.0	20.0
$H_2 - 22$	Cylindrical	0.0	2.5	150	0.0	20.0

Table 3.2 Simulation matrix - H_2 cont.

Case	Chamber	SR	TR	$u_{inj}(m/s)$	$t_{sinj}(ms)$	$t_{inj}(ms)$
$H_2 - 23$	Cylindrical - moving	0.0	0.0	300	0.0	10.0
$H_2 - 24$	Cylindrical - moving	0.5	0.0	300	0.0	10.0
$H_2 - 25$	Cylindrical - moving	1.0	0.0	300	0.0	10.0
$H_2 - 26$	Cylindrical - moving	1.5	0.0	300	0.0	10.0
$H_2 - 27$	Cylindrical - moving	2.0	0.0	300	0.0	10.0
$H_2 - 28$	Cylindrical - moving	2.5	0.0	300	0.0	10.0
$H_2 - 29$	Cylindrical - moving	0.0	0.5	300	0.0	10.0
$H_2 - 30$	Cylindrical - moving	0.0	1.0	300	0.0	10.0
$H_2 - 31$	Cylindrical - moving	0.0	1.5	300	0.0	10.0
$H_2 - 32$	Cylindrical - moving	0.0	2.0	300	0.0	10.0
$H_2 - 33$	Cylindrical - moving	0.0	2.5	300	0.0	10.0
$H_2 - 34$	Cylindrical - moving	0.0	0.0	450	6.25	6.6
$H_2 - 35$	Cylindrical - moving	0.5	0.0	450	6.25	6.6
$H_2 - 36$	Cylindrical - moving	1.0	0.0	450	6.25	6.6
$H_2 - 37$	Cylindrical - moving	1.5	0.0	450	6.25	6.6
$H_2 - 38$	Cylindrical - moving	2.0	0.0	450	6.25	6.6
$H_2 - 39$	Cylindrical - moving	2.5	0.0	450	6.25	6.6
$H_2 - 40$	Cylindrical - moving	0.0	0.5	450	6.25	6.6
$H_2 - 41$	Cylindrical - moving	0.0	1.0	450	6.25	6.6
$H_2 - 42$	Cylindrical - moving	0.0	1.5	450	6.25	6.6
$H_2 - 43$	Cylindrical - moving	0.0	2.0	450	6.25	6.6
$H_2 - 44$	Cylindrical - moving	0.0	2.5	450	6.25	6.6

3.1 KIVA

The numerical simulations were carried out using the commercial code, KIVA3V [20]. KIVA3V, written in F77, a general-purpose, procedural, imperative programming language that is especially suited to numeric computation and scientific computing, has the ability to calculate the transient three-dimensional dynamics of evaporating fuel sprays interacting with flowing multi-component gases undergoing mixing, ignition, chemical reactions, and heat transfer.

Since KIVA was developed with application to internal combustion engines in mind, it contains several features designed to facilitate such applications. However, the basic code structure is modular and quite general, and most major options (chemical reactions, sprays, etc.) can be individually activated or deactivated by setting appropriate values for the associated input switches. The code is therefore applicable to a wide variety of multi-dimensional problems in fluid dynamics, with or without chemical reactions or sprays.

KIVA solves the unsteady equations of motion of a turbulent, chemically reactive mixture of ideal gases, coupled to the equations for a single -component vaporizing fuel spray. The gas phase solution procedure is based on a finite volume method called the ALE (arbitrary Lagrangian Eulerian) method. Spatial differences are formed on a finite-difference mesh that subdivides the computational region into a number of small cells that are hexahedrons. The corners of the cells are called vertices, and the position of the vertices may be arbitrary specified functions of time, thereby, allowing a Lagrangian, Euierian, or mixed description. The arbitrary mesh can conform to curved boundaries and can move to follow changes in combustion chamber geometry. A strength of the method is that the mesh need not to be orthogonal. The spatial differencing is made conservative wherever possible. The procedure used is to difference the basic equations in integral form, with the volume of a typical cell used as the control volume, and with divergence terms transformed to surface integrals using the divergence theorem. The Cartesian components of the velocity vector are stored at cell vertices, and the momentum equations are differenced in a strictly consecrative fashion. In contrast to the original ALE method, however, cell faced velocities are used during a portion of the computational cycle. Their use greatly reduces the tendency of the ALE method to parasitic velocity modes, thereby largely eliminating the need for node coupler.

The transient solution is marched out in a sequence of finite time increments called cycle or time steps. On each cycle the value of the dependent variables are calculate from those of previous cycle. As in the original ALE method, each cycle is divided into two phases, a Lagrangian phase and a rezone phase. In the Lagrangian phase the vertices move with the fluid velocity, and there is no convection across cell boundaries. In the rezone phase, the flow field is frozen, the vertices are moved to new user-specified positions, and the flow field is remapped or rezoned onto the new computational mesh. This remapping is accomplished by convecting material across the boundaries of the computational cells, which are regarded as moving relative to the flow field [20].

The temporal difference scheme in KIVA3V is implicit. Thus, the time steps are calculated based on accuracy, not stability criteria. In the Lagrangian phase, implicit differencing is used for all the diffusion terms and the terms associated with pressure wave propagation. The coupled implicit equations are solved by a method similar to the SIMPLE algorithm, with individual equations being solved by the conjugate residual method.

Explicit methods are used to calculate convection in the rezone phase, but the convection calculation can be sub-cycled an arbitrary number of times, and thus the main computational time-step is not restricted by the Courant stability condition of explicit methods. The convection time step is a sub-multiple of the main computational time step and does satisfy the Courant condition. Partial donor cell differencing and quasi-second-order upwind (QSOU) can be used for convection. QSOU is monotone and approaches second-order accuracy when convecting smooth profiles. While more accurate than partial donor cell differencing, QSOU it is more time-consuming. In this work, partial donor cell differencing is used for convection terms.

Two models are available to represent the effects of turbulence in KIVA3V. The standard $k-\epsilon$ turbulence model is used in this study. The standard $k-\epsilon$ turbulence model was modified to include volumetric expansion effects and spray/turbulence interactions. The second turbulence model in KIVA3V is a modified version of the subgrid scale (SGS) model. The SGS model reduces to the $k-\epsilon$ model near the walls where all turbulence length scales are too small to be resolved by the computational mesh. Boundary layer drag and wall heat transfer are calculated by matching to a modified turbulent law of the wall [20, 21].

Hill and Ouellette [12], among others, have reported that the $k-\epsilon$ turbulence model leads to an over-estimation of the spreading rate (jet half width / distance from the nozzle) of steady-state turbulent jets. For round free jets of air into air, the turbulence model is reported to predict a spreading rate of 0.11, while the accepted experimental value is $0.085 - 0.09$. The reason for the inaccuracy is related to the assumption of isotropy in modeling the turbulence. The assumption apparently does not hold for jets, in which normal strain differ from aligned strain. Although algebraic corrections have been proposed for steady-state turbulent jet modeling, they require knowledge of the jet centerline location and conditions. This may be difficult to obtain in complex, varying geometries such as engine combustion chambers. The equations of motion of the fluid phase and boundary conditions employed in KIVA3V are given in Appendix A.

The error in the calculation for all the variables is 10^{-3} except pressure 10^{-4}. These are the values recommended by KIVA. If tighter convergence is needed less values are advised. The time step in each cycle is set to be 10^{-4}.

3.2 Computational Geometries

Two fixed volume chambers and one variable volume chamber with moving piston are the geometries used to study mixture formation in a transient gaseous fuel jet injection, as shown in Figure 3.1. Cubic and cylindrical chambers are considered as the constant volume chambers. Their dimensions were chosen so that the total volume to be the same. The cube has the dimensions of $10\,cm \times 10\,cm \times 10\,cm$, the diameter of the cylinder is $10\,cm$ with the height of $12.73\,cm$, making the total volume of each chamber, $1\,L$. The variable volume chamber has the same dimension as the fixed cylindrical chamber when the piston is at bottom dead center (BDC). The stroke is $11.457\,cm$ and the clearance height is $1.273\,cm$, giving the compression ratio of 10 ($r_v = 10$). The crankshaft rotates with an rpm of 2400.

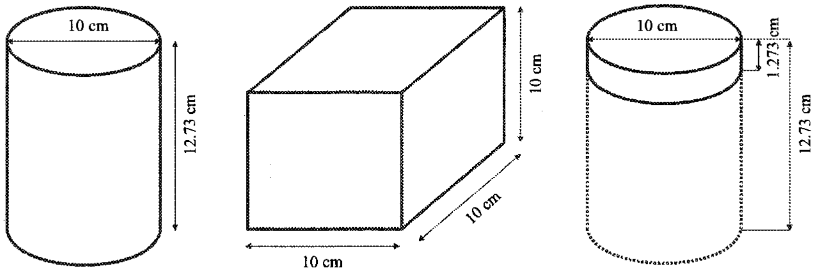

Fig. 3.1: Fixed and variable volume chambers

The injector is located on the top wall of the chambers with a radius of $4\,mm$. In the fixed chamber a group of 6×6 cells are used to mesh the injector, while for variable volume chamber 8 cells were used across the injector.

In mesh sensitivity analysis section the effect of number of nodes along each side of the cubic and cylindrical chamber on volume of flammable mixture is examined.

3.3 Boundaries and Initial Conditions

The initial and boundary conditions employed in the numerical simulation are listed in Table 3.3 for the air inside the chamber, and Table 3.4 for the transient gaseous fuel jet. Before injection occurs, a bulk motion of air was provided using a Bessel function to represent velocity profile. The reference engine *rpm* used in this study is 2400. Therefore, the angular momentum provided by the bulk motion of air is defined relative to angular momentum of air in an engine runs on *rpm* of 2400.

Table 3.3: Boundary conditions for chamber walls and air inside the chamber

Chamber walls temperature	$293.15\,K$
Air temperature	$293.15\,K$
Air pressure	$1.0 \times 10^5\,Pa$
Air composition (mass fraction)	
O_2	0.22
N_2	0.76
CO_2	0.13
H_2O	0.09
Turbulent kinetic energy	$0.1\,cm^2/s^2$
Turbulent length scale	$0.1\,cm$

Table 3.4: Boundary and initial conditions for the gaseous fuel jet

Injection velocity	$150\,m/s - 450\,m/s$
Temperature	$293.15\,K$
Pressure	$1.0 \times 10^5\,Pa$
Turbulent length scale	$0.1\,cm$

Bessel-function bulk motion of air velocity profile

Internal combustion engines are designed to create a significant amount of swirl/tumble in the incoming air, to aid in turbulent mixing and enhance combustion efficiency. The simplest model assumes that the swirl/tumble velocity has a wheel-flow profile, but this is not usually a realistic assumption, as the turbulent wall boundary layer forces the swirl/tumble velocity to decrease in the wall region. From experimental observation, modelers have determined that a Bessel function profile more accurately represents the flow. Figure 3.2 illustrates the Bessel function velocity profile provided in KIVA and compares it with wheel flow for the same swirl number. The quantity α is a dimensionless constant that defines the initial azimuthal velocity profile and lies between 0.0 (the wheel flow limit) and 3.83 (zero velocity at the wall). A value suggested by Wahiduzzaman and Ferguson [22] for typical engine applications is about 3.11. The Bessel function profile is defined so that it gives the same angular momentum as wheel flow with the same swirl number. Thus, the initial slope of the $\alpha = 3.11$ curve is necessarily higher than the corresponding slope for wheel flow.

A second input quantity, SWIRL, is the initial swirl ratio of air *rpm* to crankshaft *rpm*. On the other hand, it indicates how much faster the bulk motion of air is rotating compare to engine *rpm*.

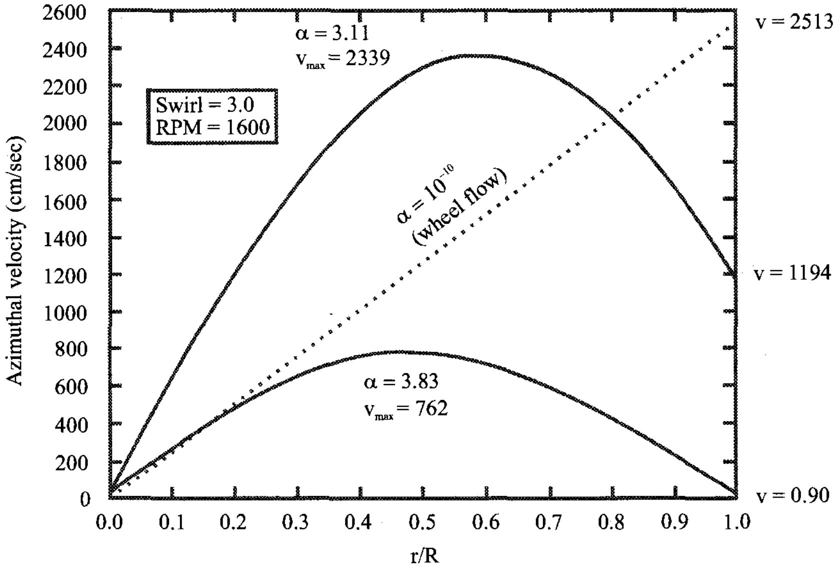

Fig. 3.2: Bessel function swirl velocity profile provided in KIVA setup.

In Figure 3.3 the streamlines of bulk motion of air are shown at the initial time.

Considering the fact that tumble and swirl ratios are defined based on engine *rpm*, an arbitrary tumble and swirl ratio were defined for the fixed cubic volume cases. Thus, in fixed cubic and cylindrical chambers, the angular momentum of air inside the chamber corresponds to an engine working with the *rpm* of 2400 as a reference engine speed.

The general formula for the Bessel function appearing in angular momentum is given by,

$$a = \frac{2}{\alpha} J_1(\alpha) - J_0(\alpha) \tag{3.1}$$

where J_1 and J_0 are the Bessel functions of order one and zero respectively. The value of 3.11 is used for α in the calculations.

The zero and first order Bessel functions are approximated as follows [21],

$$J_n(x) = \begin{cases} \frac{(r_1+x^2(r_2+x^2(r_3+x^2(r_4+x^2(r_5+r_6x^2)))))}{(s_1+x^2(s_2+x^2(s_3+x^2(s_4+x^2(s_5+s_6x^2)))))} & |x| \leq 8.0 \\ \\ \sqrt{0.636619772/ax}(\cos(xx_n)(p_1+y(p_2+y(p_3+y(p_4+p_5y)))) & \\ -z\sin(xx_n)(q_1+y(q_2+y(q_3+y(q_4+yq_5))))) & |x| > 8.0 \end{cases} \tag{3.2}$$

where

$$\begin{aligned} ax &= |x| \\ z &= 8.0/|x| \\ y &= z^2 \\ xx_0 &= |x| - 0.7854 \end{aligned} \tag{3.3}$$

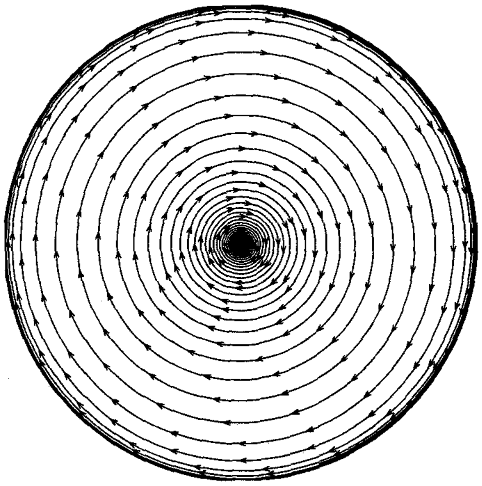

(a)

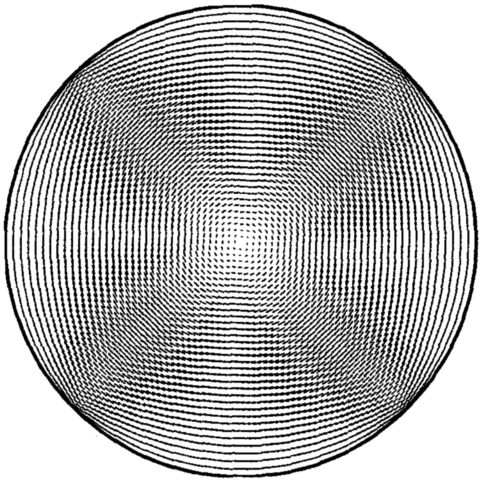

(b)

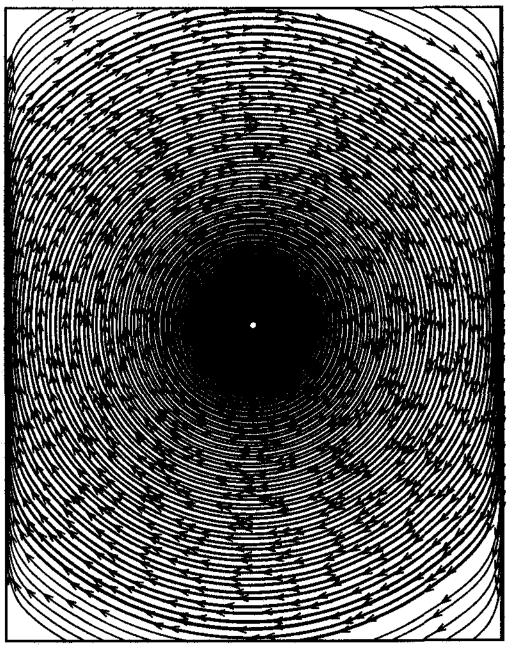

(c)

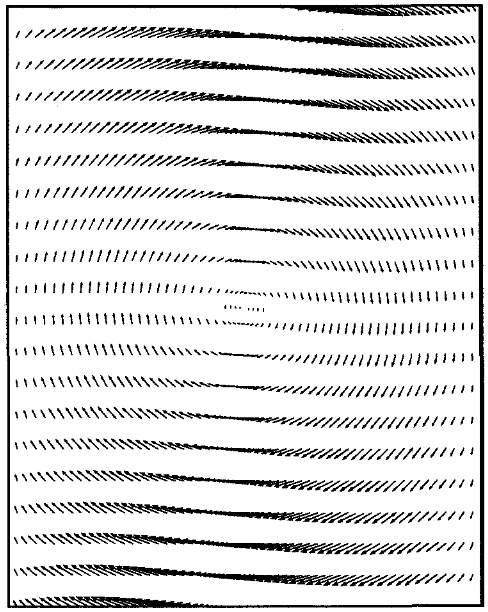

(d)

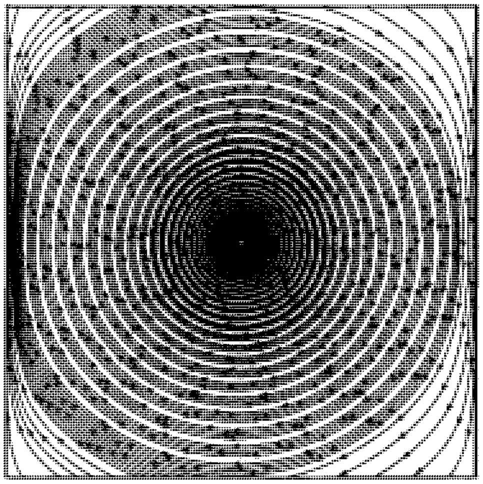

(e)

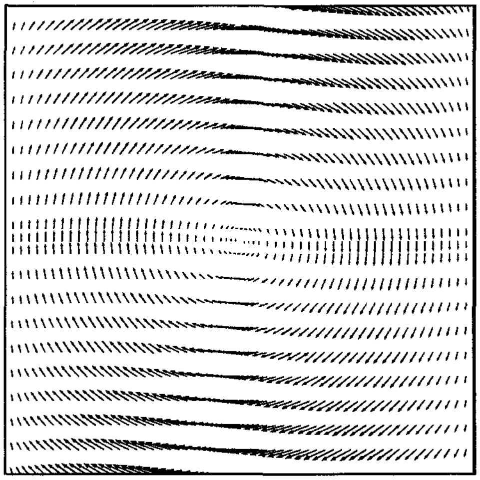

(f)

Fig. 3.3: Streamlines and velocity profile of bulk motion of air at the initial time. (a),(b) swirl profile in cylindrical chamber, (c),(d) tumble profile in cylindrical chamber, (e),(f) tumble/swirl profile in cubic chamber.

$$xx_1 = |x| - 2.3562$$

The constants p_i, q_i, r_i, s_i are listed in Table 3.5.

Table 3.5: Constants used in Bessel functions approximations

	p_1	p_2	p_3	p_4	p_5	
J_0	1.0	-1.0986e-03	2.7345e-05	-2.0733e-06	2.0938e-07	
J_1	1.0	1.8310e-03	-3.5163e-05	2.4575e-06	-2.4033e-07	
	q_1	q_2	q_3	q_4	q_5	
J_0	-1.5624e-02	1.4304e-04	-6.9111e-06	7.6210e-07	-9.3494e-08	
J_1	4.6874e-02	-2.0026e-04	8.4491e-06	-8.8228e-07	1.0578e-07	
	r_1	r_2	r_3	r_4	r_5	r_6
J_0	5.7568e+10	-1.3362e+10	6.5161e+08	-1.1214e+07	7.7393e+04	-1.8490e+02
J_1	7.2362e+10	-7.8950e+09	2.4239e+08	-2.9726e+06	1.5704e+04	-3.0160e+01
	s_1	s_2	s_3	s_4	s_5	s_6
J_0	5.7568e+10	1.0295e+09	9.4946e+06	5.9272e+04	2.6785e+02	1.0
J_1	1.4475e+11	2.3005e+09	1.8583e+07	9.9447e+04	3.7699e+02	1.0

Gaseous injection model

The original KIVA3V code is only able to model liquid fuel sprays and does not support gaseous fuel injection. Thus, for this study, the original code has been modified and several subroutines have been added to the original code to make gaseous fuel injection possible.

A group of 6×6 cells for fixed volume and 8×8 for variable volume chamber located on the top wall of the chambers, are selected to represent the circular cross section of the injector nozzle exit. These cells will be referred to as 'injector cells'. The radius of the nozzle exit is $4mm$. Gas injection occurs through a constant-velocity boundary. This is done by specifying the faces of the injector cells as inflow boundary supplying normal velocity of U_{inj} (injection velocity).

Additional properties are also required for gaseous injection such as specific turbulent kinetic energy k_0, length scale $l_{\epsilon 0}$, and reference species mass density ρ_{m0}. The reference density of different species is at reference pressure P_0 and the density imposed at the inflow boundary for species m is obtained from [20],

$$\rho_{m,in} = \rho_{m0}(p/p_0)^{1/\gamma_{amb}} \tag{3.4}$$

where p is the calculated pressure in the injection cells and γ_{amb} is the ratio of specific heats of the inflow gas. Therefore, the species mass fraction and the entropy of the incoming fluid at the inflow boundary are imposed with the densities obtained by extrapolation from isentropic gas relation. The gas pressure is calculated by

$$p = R_0 T \sum_m (\rho_m / W_m). \tag{3.5}$$

The inflow internal energies are obtained from pressure p and densities $\rho_{m,in}$ using the state equation,

$$I(T) = R_0 T \sum_m (\rho_m / \rho).I_m(T) \tag{3.6}$$

For computational time lies between t_{sinj} (start of injection) and $t_{sinj} + t_{inj}$, injection parameters are introduced as source terms into boundary cells of the computational domain, the injector cells. Injection mass within the interval of $[t_{sinj}, t_{sinj} + t_{inj}]$ is updated using the following equations,

$$\rho_{ic,n+1} = \rho_{ic,n} + \frac{\dot{m}_{in}.dt}{vol_{ic,n}} \tag{3.7}$$

$$\rho_{m,ic,n+1} = \rho_{m,ic,n} + \frac{\dot{m}_{in}.dt}{vol_{ic,n}} \tag{3.8}$$

$$\dot{m}_{in} = \rho_{in} A U_{inj} \tag{3.9}$$

$$m_{ic,n} = \rho_{ic,n}.vol_{ic,n} \tag{3.10}$$

$$m_{ic,n+1} = \rho_{ic,n+1}.vol_{ic,n} \tag{3.11}$$

where 'ic' denotes "injector cells". The velocity has only normal component to the injector cells,

$$\mathbf{u}_{ic,n+1} = \mathbf{u}_{ic,n} = U_{inj}.\mathbf{b} \tag{3.12}$$

where **b** is the normal vector to the injector cells.

3.4 Mesh Sensitivity

It is generally agreed that adequate resolution is required to reproduce the structure of gas jets in numerical computations. Abraham [23] concluded that the resolution appears to be adequate for gaseous jets when the grid size is at least the size of orifice radius. This suggests that at least two cells across the nozzle exit are required. Hill and Ouellette [12] conducted numerical experiments regarding the grid size effect and concluded that changing number of cells within the nozzle from two to four caused only 1 % reduction in the normalized penetration rate.

The effect of grid size on flammable mixture volume was studied by generating two adjustable cubic and cylindrical chambers, as shown in Figure 3.4. The two chambers were generated for the purpose of mesh sensitivity analysis in K3PREP, the mesh generation package available in KIVA3V. The cubic chamber consisted of 27 blocks patched together. Distribution of the nodes is uniform. The cylindrical chamber had 3 blocks in 3 rows. The radius and height are the parameters that can be specified. The results of mesh sensitivity analysis are shown in Table 3.6 and Table 3.7 for cubic and cylindrical chambers, respectively. The length of each segment and the number of nodes used to nodes along them are shown for each case are listed. In the first two cases, the mesh is finer near the injector but in the third case the grid is uniform. The results show that the volume of flammable mixture changes slightly when the finer mesh is used. Number of cells across the nozzle as mentioned before is good enough to model the mixing process.

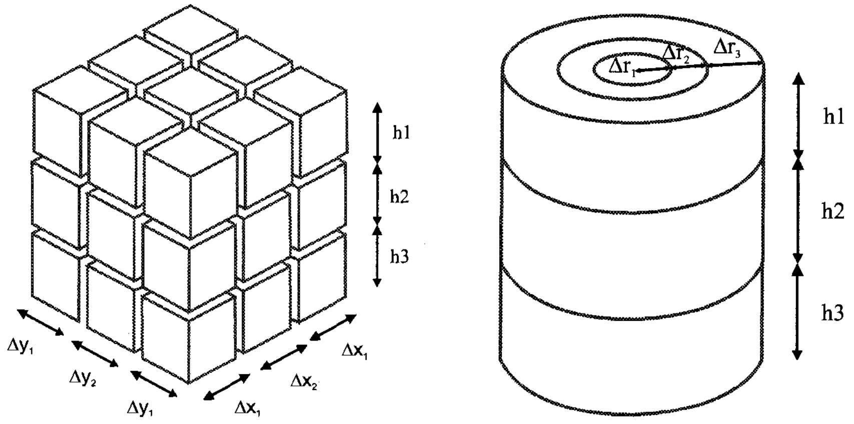

(a) (b)

Fig. 3.4: Two geometries used to study mesh sensitivity

Table 3.6: Result of mesh sensitivity analysis for cubic mesh

	case i	*case ii*	*case iii*
$\Delta x_1 = \Delta y_2$	40 mm/32	40 mm /26	40 mm/40
$\Delta x_2 = \Delta y_1$	20 mm/18	20 mm/16	20 mm/20
h_1	10 mm/9	20 mm/17	30 mm/30
h_2	40 mm/33	40 mm/30	30 mm/30
h_3	50 mm/38	40 mm/28	30 mm/30
N_{inj}	8	6	8
$V_{flammable}$	87.5%	87.9%	88.1%

Table 3.7: Result of mesh sensitivity analysis for cylindrical mesh

	case i	*case ii*	*case iii*
Δr_1	10 mm/9	20 mm 17	10 mm/10
Δr_2	40 mm/34	40 mm/30	40 mm,40
Δr_3	50 mm/38	40 mm/28	50 mm/50
h_1	10 mm/9	20 mm/17	30 mm/30
h_2	40 mm/33	40 mm/30	30 mm/30
h_3	50 mm/38	40 mm/28	30 mm/30
N_{inj}	8	6	8
$V_{flammable}$	96.2%	95.1%	97.1%

Chapter 4

Results

4.1 Volume of flammable mixture for fixed volume chambers

Volume of flammable mixture is plotted versus time in Figures 4.1 to 4.8 for the fixed volume chambers at six different levels of angular momentum. The injection duration for methane and hydrogen is $10\,ms$ and $20\,ms$ respectively. The start of injection is from time 0. After the end of injection, the mixture formation between air inside the chamber and injected methane continues for another $30\,ms$, and for $50\,ms$ for hydrogen jet. Thus, the total simulation time is $40\,ms$ and $70\,ms$. The results show that the process of mixing can be divided into two stages. The first stage happens during injection of fuel. In this stage, most of the mixing has taken place. In the second stage which mixture formation is slower than the first stage, the mixing process is more dependent on the momentum of the bulk motion. It should be noted that, because of the very short time of injection, diffusion process does not have a significant effect in the mixing process.

Mixing of hydrogen and air in all the cases is faster and more dependent on ASR or ATR. It is worthwhile to mention that the flammable limit of hydrogen covers a wider range of equivalence ratios $(0.1-7.1)$ than does methane $(0.5-2)$. That is the main reason that makes the creation of flammable mixture faster for hydrogen tahn with methane.

The effect of geometry on mixture preparation is studied using two different geometries, cubic and cylindrical. The total volume of each chamber is 1 L. The results for injection of hydrogen and methane in the cubic and cylindrical chamber show that mixture formation in the cylindrical chamber is much faster than in the cubic chamber and also mixing is greatly affected by the molecular weight of gaseous fuel. In Figures 4.10 and 4.11, the contour of mass fraction and streamlines are shown. It is clear that the bulk motion of air pushes methane to the wall and makes a very rich region near the wall while it traps hydrogen in a cylindrical shape region filled with fuel. Another drawback of the cubic chamber that should be mentioned are the four sharp corners of the cube. At some ASR or ATR, the fuel is trapped in the small vortices in the corners and does not take part in mixture formation.

Figures 4.12 to 4.15 compare volume of flammable mixture at two minimum and maximum tumble and swirl ratios for hydrogen and methane. In the cubic chamber the mixing formation of methane at minimum and maximum ASR and ART is similar to that of hydrogen where there is no bulk motion. As mentioned earlier, molecular weight of the injected fuel plays the important role during mixture formation in the cubic chamber.

Figure 4.12 and Figure 4.14 show flammable mixture volume has slightly changes for different level of tumble or swirl ratio . From an engine point of view, although methane does not create a flammable mixture in the cubic chamber as in the cylindrical chamber, the distribution of fuel and creation of a rich region near the wall, makes the cubic chamber a good choice for applications where stratified charge is needed near the spark plug. The purpose behind stratified charge engines is to have a readily ignitable mixture in the vicinity of the spark plug, and a weaker (possibly non-ignitable) mixture in the reminder of the combustion chamber.

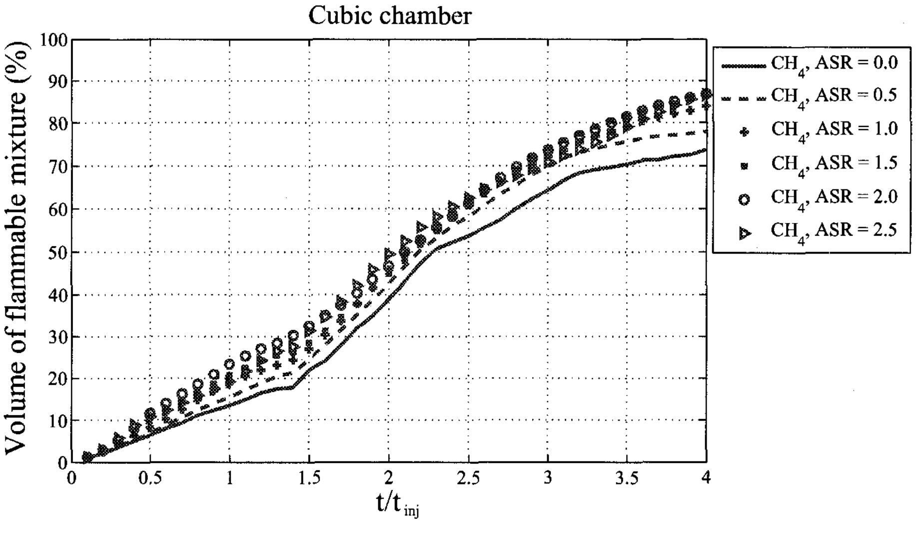

Fig. 4.1: Volume of flammable mixture vs. time at different swirl ratios in constant cubic volume chamber; $U_{inj} = 150\,m/s$, $t_{inj} = 10\,ms$, $t_{sinj} = 0$.

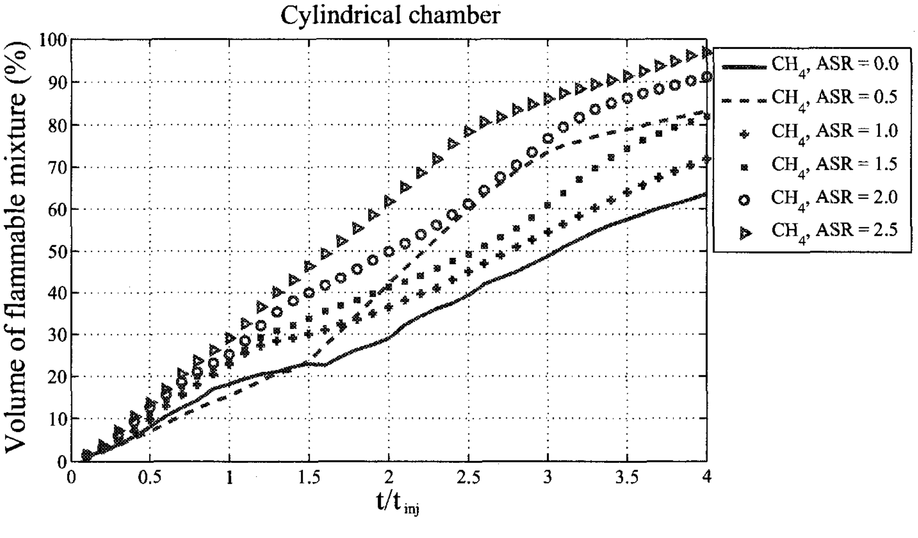

Fig. 4.2: Volume of flammable mixture vs. time at different swirl ratios in constant cylindrical volume chamber; $U_{inj} = 150\,m/s$, $t_{inj} = 10\,ms$, $t_{sinj} = 0$.

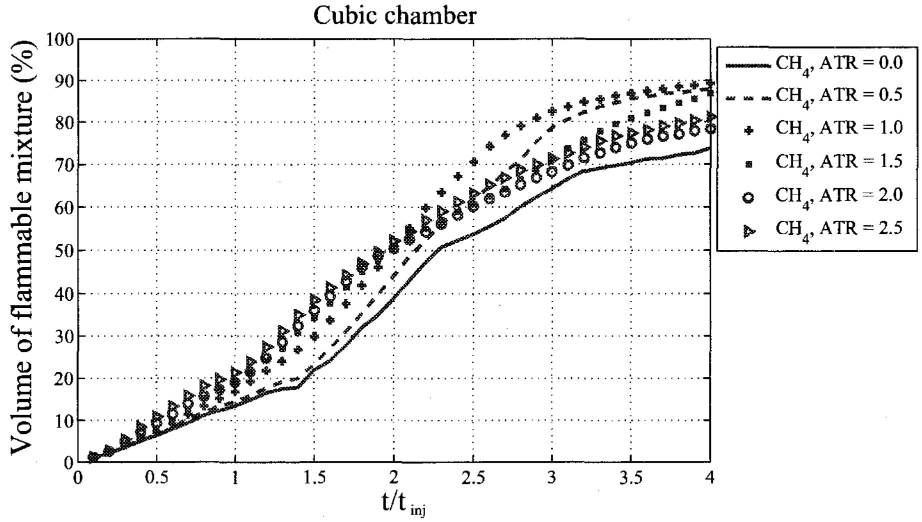

Fig. 4.3: Volume of flammable mixture vs. time at different tumble ratios in constant cubic volume chamber; $U_{inj} = 150\,m/s$, $t_{inj} = 10\,ms$, $t_{sinj} = 0$.

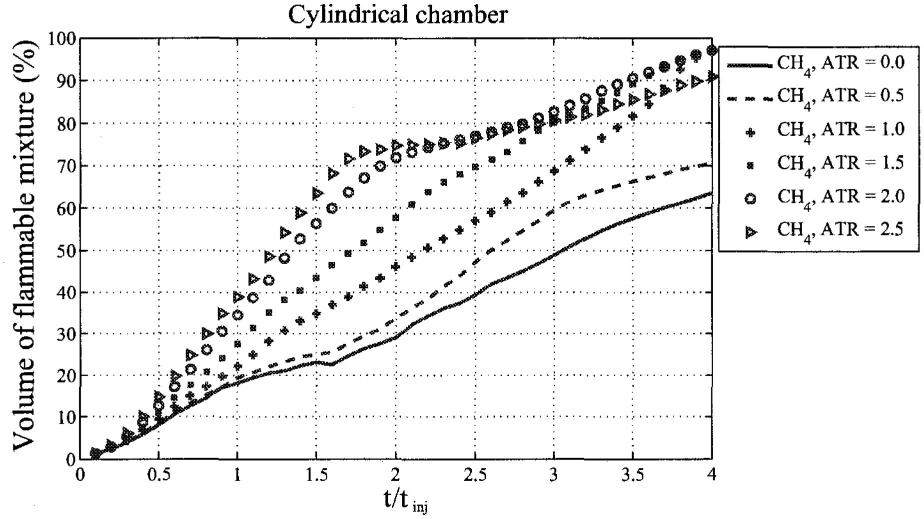

Fig. 4.4: Volume of flammable mixture vs. time at different tumble ratios in constant cylindrical volume chamber; $U_{inj} = 150\,m/s$, $t_{inj} = 10\,ms$, $t_{sinj} = 0$.

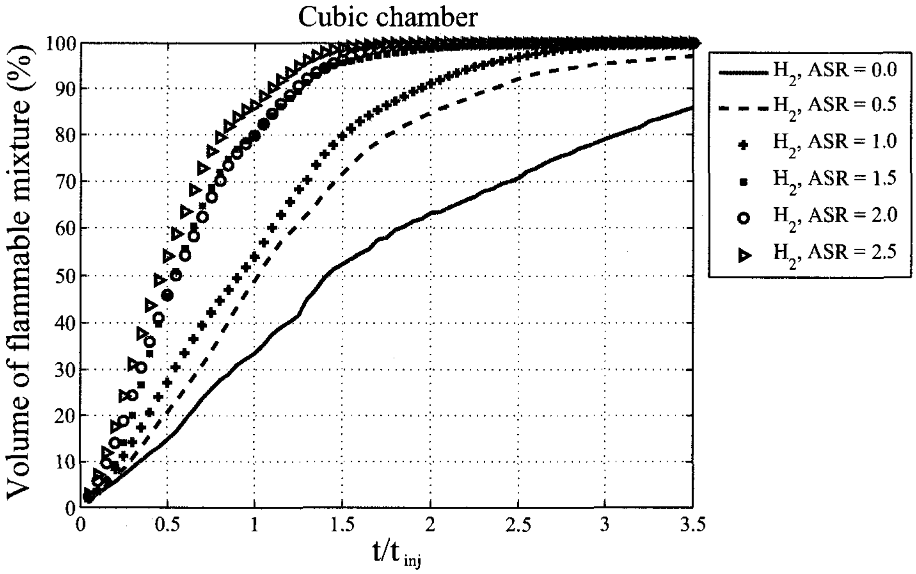

Fig. 4.5: Volume of flammable mixture vs. time at different swirl ratios in constant cubic volume chamber; $U_{inj} = 150\,m/s$, $t_{inj} = 20\,ms$, $t_{sinj} = 0$.

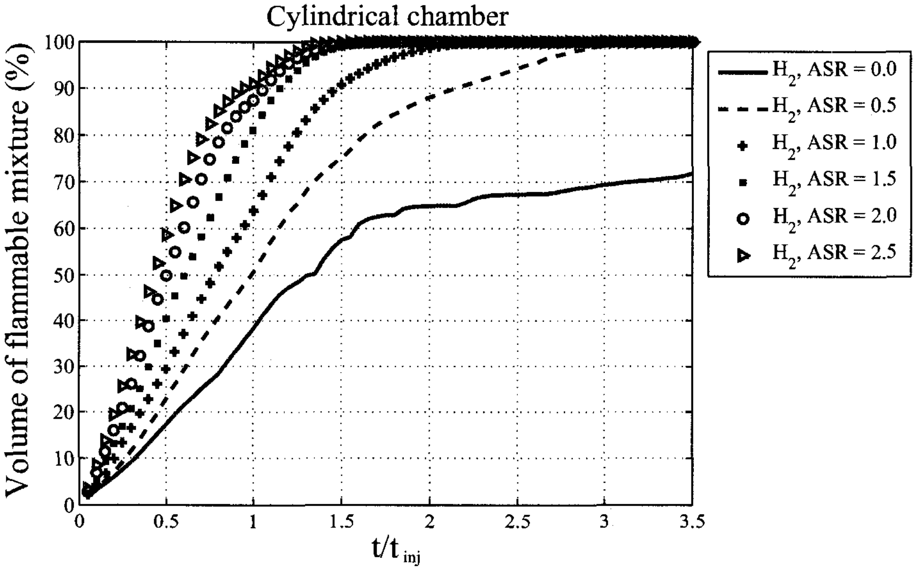

Fig. 4.6: Volume of flammable mixture vs. time at different swirl ratios in constant cylindrical volume chamber; $U_{inj} = 150\,m/s$, $t_{inj} = 20\,ms$, $t_{sinj} = 0$.

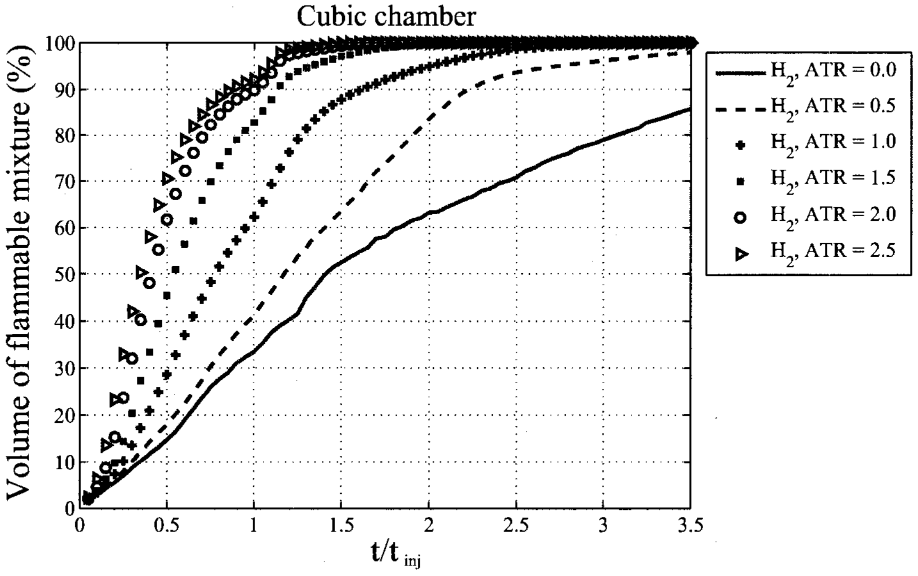

Fig. 4.7: Volume of flammable mixture vs. time at different tumble ratios in constant cubic volume chamber; $U_{inj} = 150\,m/s$, $t_{inj} = 20\,ms$, $t_{sinj} = 0$.

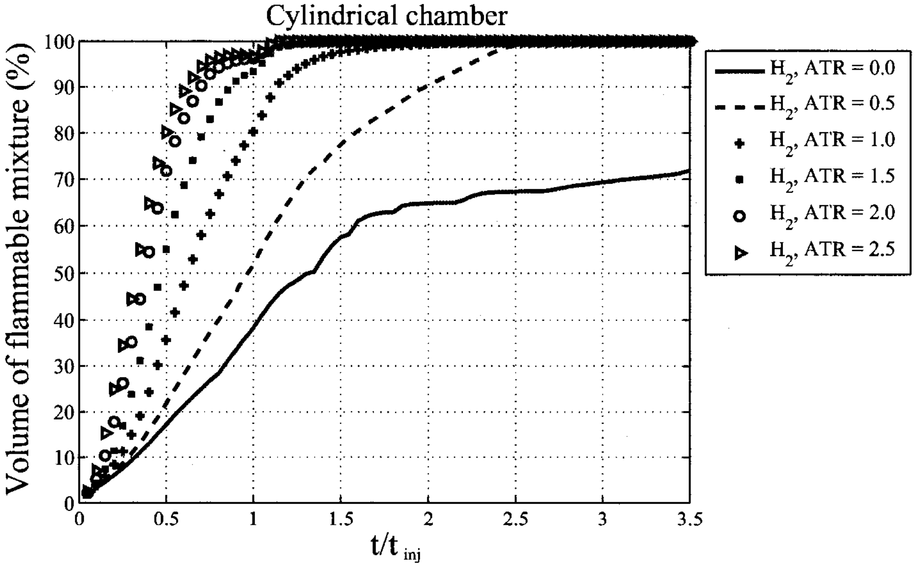

Fig. 4.8: Volume of flammable mixture vs. time at different tumble ratios in constant cylindrical volume chamber; $U_{inj} = 150\,m/s$, $t_{inj} = 20\,ms$, $t_{sinj} = 0$.

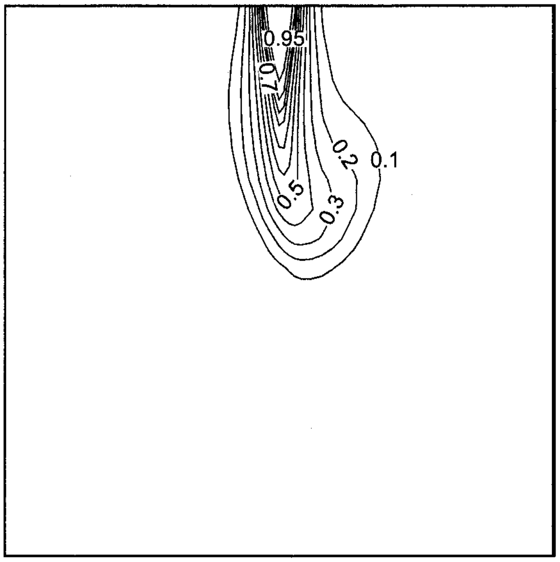

(a) $t = 0$

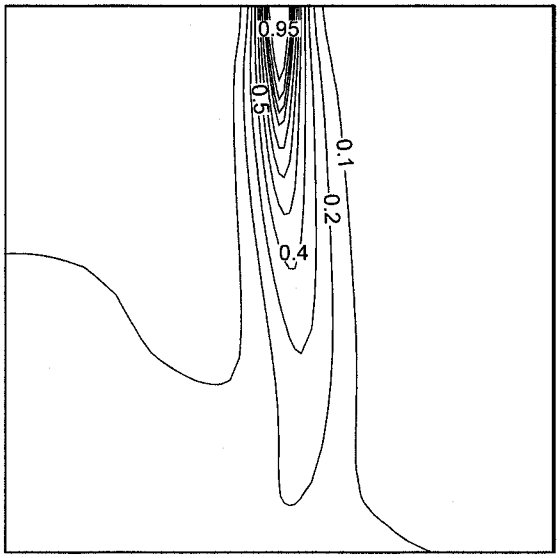

(b) $t = 10\,ms$

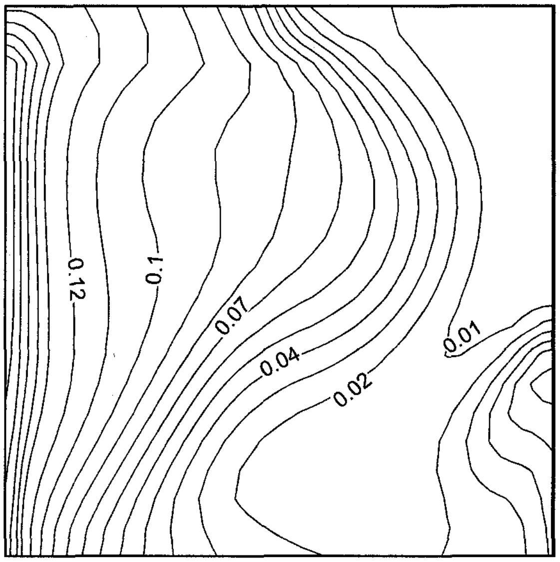

(c) $t = 20\,ms$

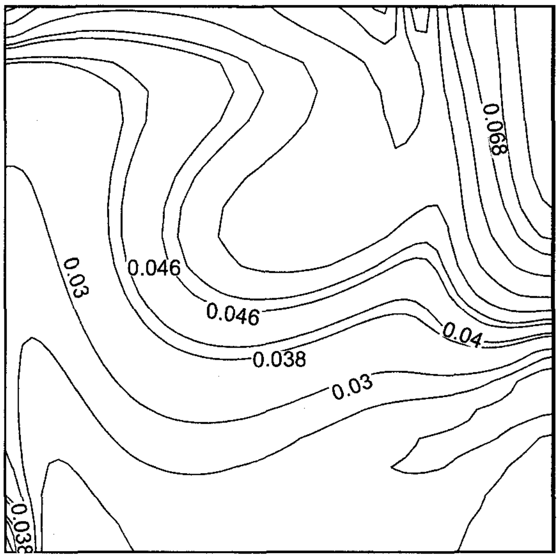

(d) $t = 40\,ms$

Fig. 4.9: Mass fraction contours of CH_4 in a plane cut through the injector at different times; $ASR = 3$, $U_{inj} = 150\,m/s$, $t_{inj} = 10\,ms$, $t_{sinj} = 0$.

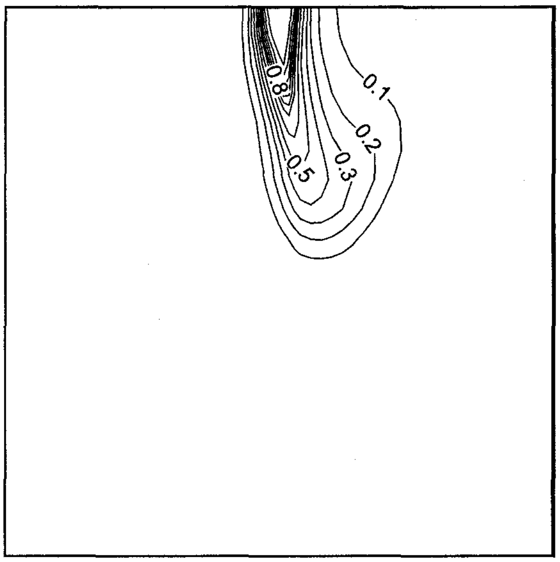

(a) $t = 0$

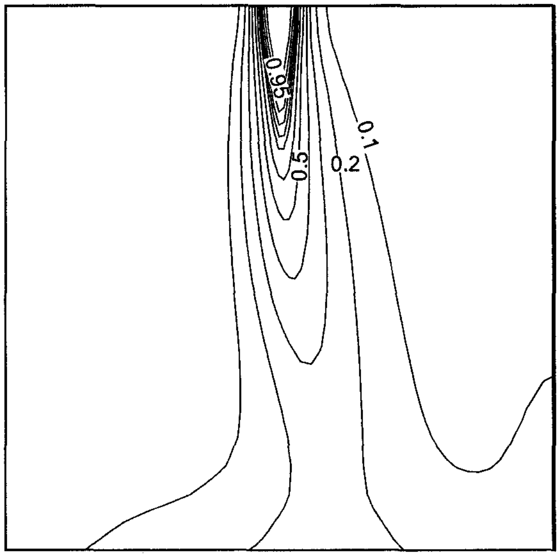

(b) $t = 10\,ms$

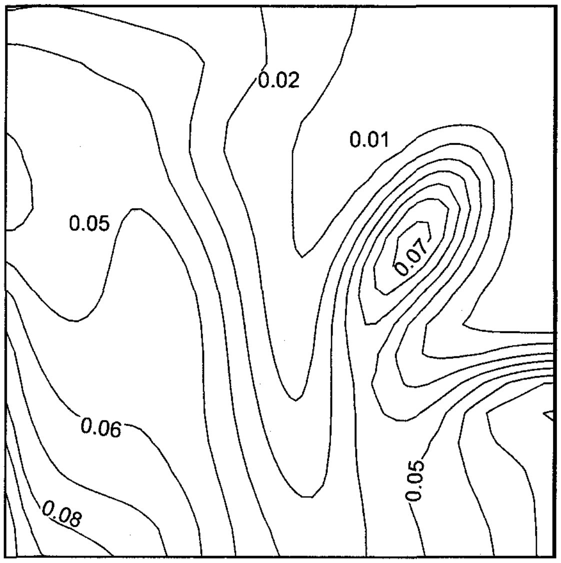

(c) $t = 20\,ms$

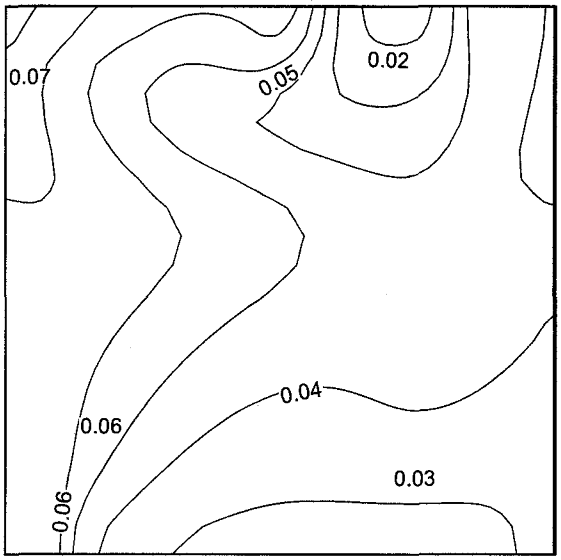

(d) $t = 40\,ms$

Fig. 4.10: Mass fraction contours of CH_4 in a plane cut through the injector at different times; $ATR = 3$, $U_{inj} = 150\,m/s$, $t_{inj} = 10\,ms$, $t_{sinj} = 0$.

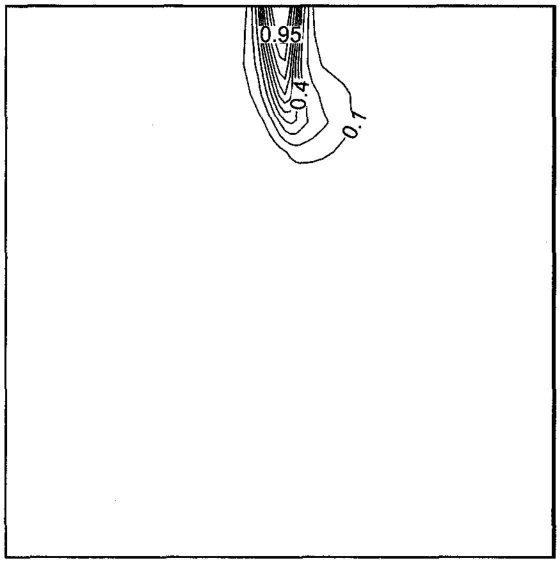

(a) $t = 0$

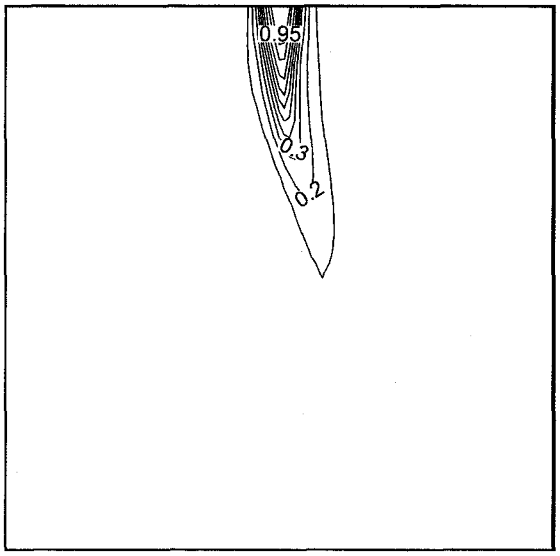

(b) $t = 10\,ms$

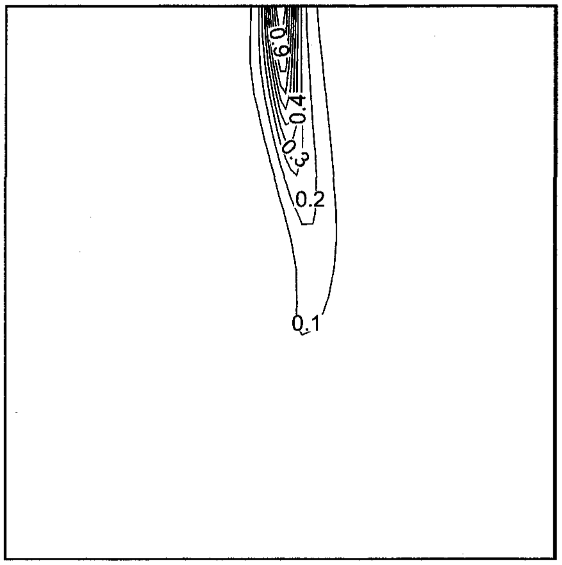

(c) $t = 20\,ms$

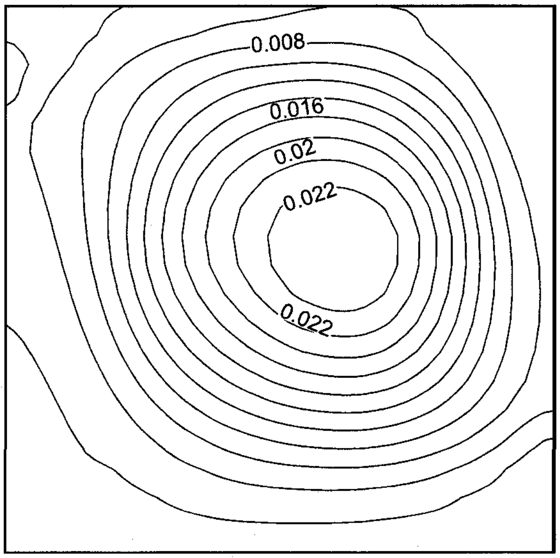

(d) $t = 40\,ms$

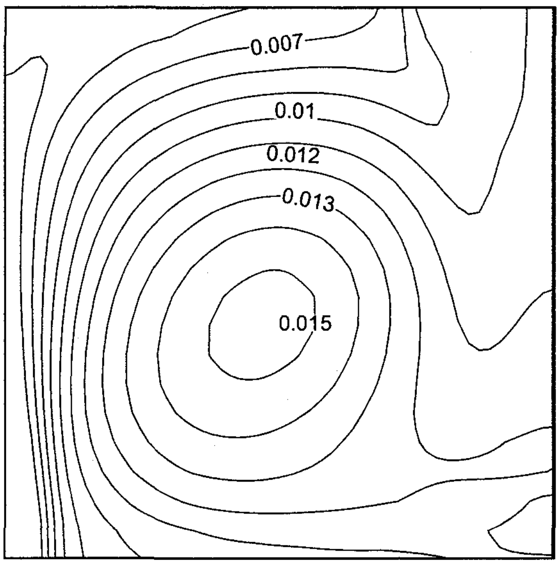

(e) $t = 70\,ms$

Fig. 4.11: Mass fraction contours of H_2 in a plane cut through the injector at different times. $ATR = 3$, $U_{inj} = 150\,m/s$, $t_{inj} = 20\,ms$, $t_{sinj} = 0$.

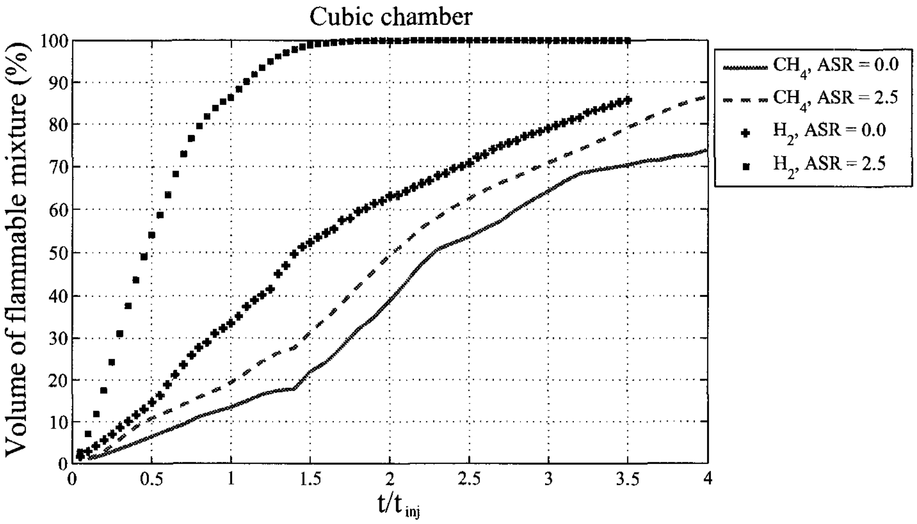

Fig. 4.12: Comparison of flammable mixture formation between H_2 and CH_4 at two different swirl ratios in cubic constant volume chamber; CH_4: $U_{inj} = 150\,m/s$, $t_{inj} = 10\,ms$, $t_{sinj} = 0$; H_2: $U_{inj} = 150\,m/s$, $t_{inj} = 20\,ms$, $t_{sinj} = 0$.

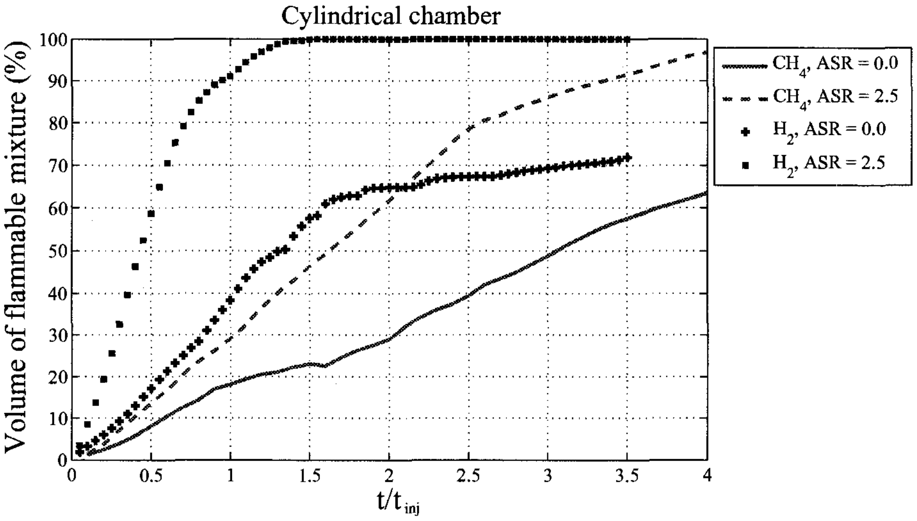

Fig. 4.13: Comparison of flammable mixture formation between H_2 and CH_4 at two different swirl ratios in cylindrical constant volume chamber; CH_4: $U_{inj} = 150\,m/s$, $t_{inj} = 10\,ms$, $t_{sinj} = 0$; H_2: $U_{inj} = 150\,m/s$, $t_{inj} = 20\,ms$, $t_{sinj} = 0$.

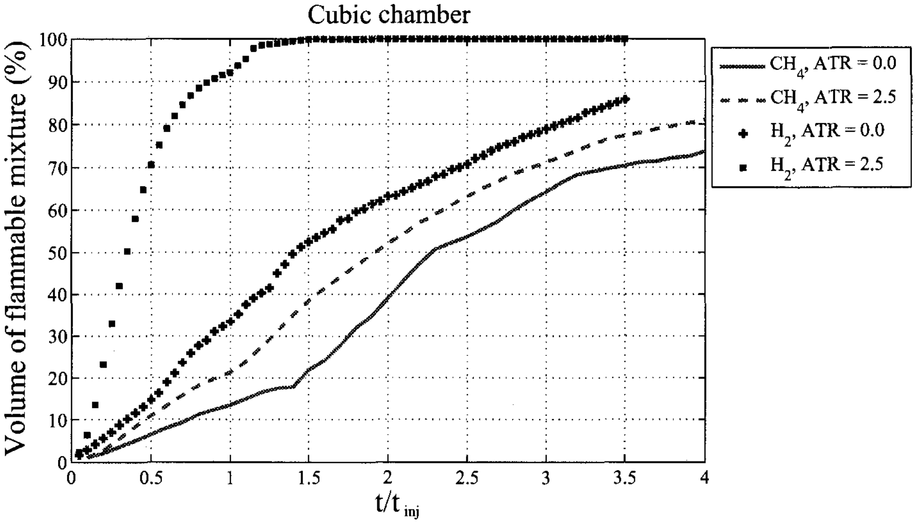

Fig. 4.14: Comparison of flammable mixture formation between H_2 and CH_4 at two different tumble ratios in cubic constant volume chamber; CH_4: $U_{inj} = 150\,m/s$, $t_{inj} = 10\,ms$, $t_{sinj} = 0$; H_2: $U_{inj} = 150\,m/s$, $t_{inj} = 20\,ms$, $t_{sinj} = 0$.

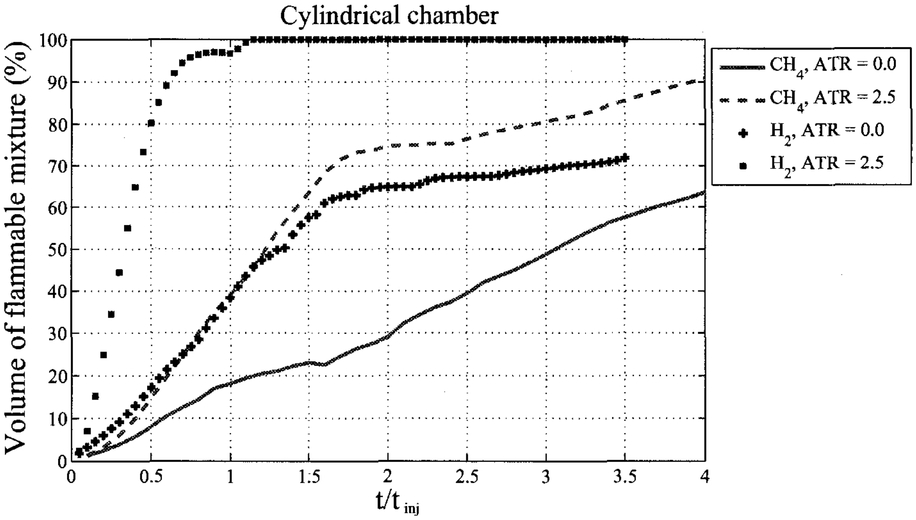

Fig. 4.15: Comparison of flammable mixture formation between H_2 and CH_4 at two different tumble ratios in cylindrical constant volume chamber; CH_4: $U_{inj} = 150\,m/s$, $t_{inj} = 10\,ms$, $t_{sinj} = 0$; H_2: $U_{inj} = 150\,m/s$, $t_{inj} = 20\,ms$, $t_{sinj} = 0$.

4.2 Volume of flammable mixture for variable volume chamber

The impact of a moving piston on mixture formation is simulated only in the cylindrical chamber. The crankshaft rotates with *rpm* of 2400. There are two sets of results. In the first set, the start of injection is at the start of simulation ($t_{sinj} = 0$), whith the piston is located at BDC. In the second case, the injection starts when the piston has moved half way up, ($t_{sinj} = 6.25\,ms$). The results presented here are at 6 tumble/swirl ratios for the both sets.

Figures 4.16 to 4.19 show the volume of flammable mixture vs. time for methane and hydrogen at different swirl ratios. For both gases, increasing the level of swirl does not lead to better distribution of fuel. The reason is that while the piston moves up because angular momentum should be conserved, it makes the bulk motion of air rotate faster. The fuel is trapped inside the bulk motion and there is less chance to mix with surrounding air. On the other hand, having a greater level of tumble helps the mixing process, as shown in Figure 4.17 and Figure 4.19.

The effects of start of injection , t_{sinj}, is presented in Figures 4.20 to 4.23. The results show the same behavior of flammable mixture formation as when the injection begins at $t_{sinj} = 0$ and swirl motion is present in the chamber. But there are no changes in volume of flammable mixture when different levels of tumble are imposed inside the chamber. The main reason for this is the disappearance of tumbling motion in the compression stroke. This will be discussed when the results showing the decay of angular momentum are presented.

The volume of flammable mixture at maximum and minimum swirl and tumble ratio are shown in Figures 4.24 to 4.27 for two different injection time. Mixing of hydrogen and air in all cases are faster than methane and air. It is also clear mixture formation during late injection is faster when the fuel was injected at $t = 0$.

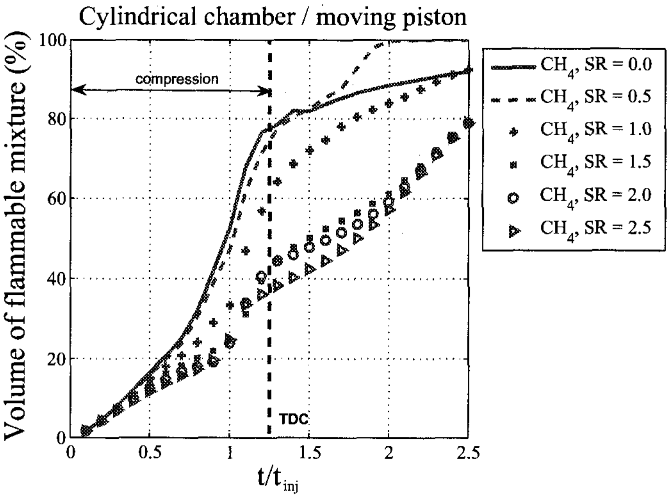

Fig. 4.16: Volume of flammable mixture vs. time at different swirl ratios in cylindrical chamber with moving piston; $U_{inj} = 150m/s$, $t_{inj} = 10ms$, $t_{sinj} = 0$.

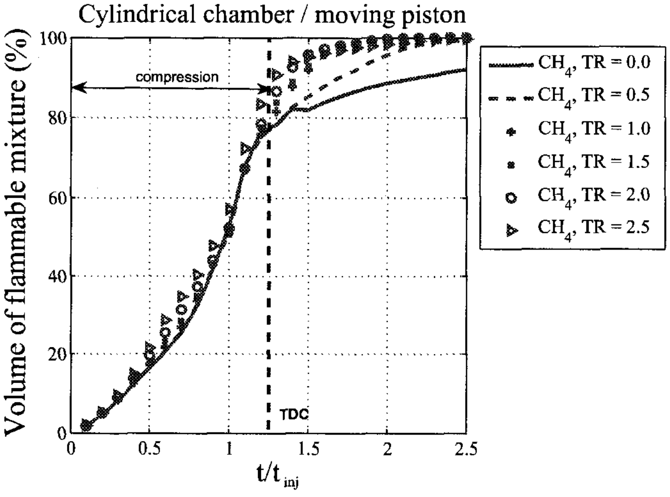

Fig. 4.17: Volume of flammable mixture vs. time at different tumble ratios in cylindrical chamber with moving piston; $U_{inj} = 150m/s$, $t_{inj} = 10ms$, $t_{sinj} = 0$.

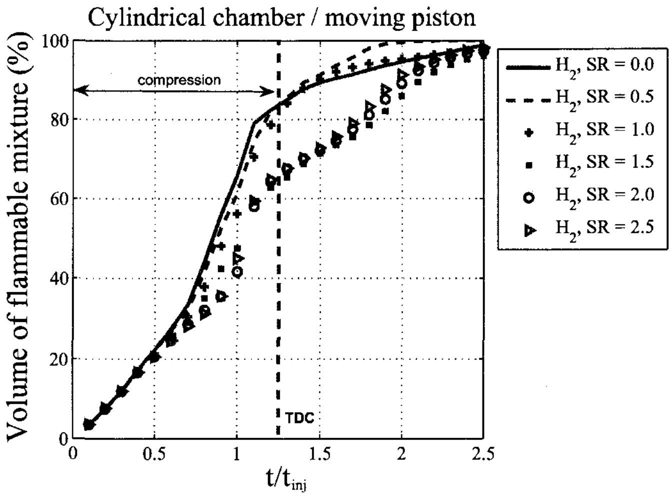

Fig. 4.18: Volume of flammable mixture vs. time at different swirl ratios in cylindrical chamber with moving piston; $U_{inj} = 300m/s$, $t_{inj} = 10ms$, $t_{sinj} = 0$.

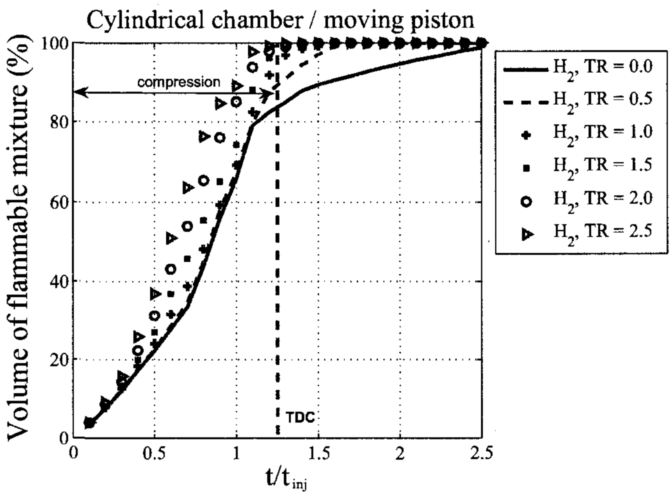

Fig. 4.19: Volume of flammable mixture vs. time at different tumble ratios in cylindrical chamber with moving piston; $U_{inj} = 300m/s$, $t_{inj} = 10ms$, $t_{sinj} = 0$.

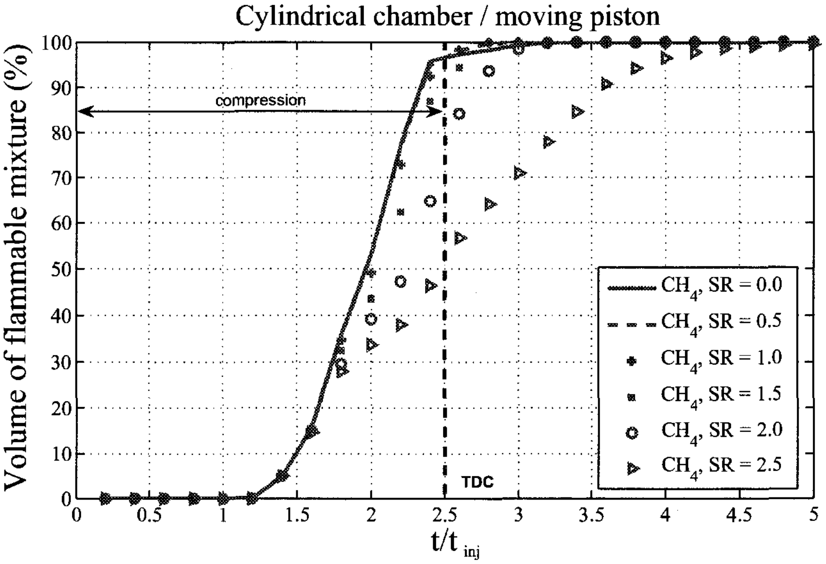

Fig. 4.20: Volume of flammable mixture vs. time at different swirl ratios in cylindrical chamber with moving piston; $U_{inj} = 300m/s$, $t_{inj} = 5ms$, $t_{sinj} = 6.25ms$.

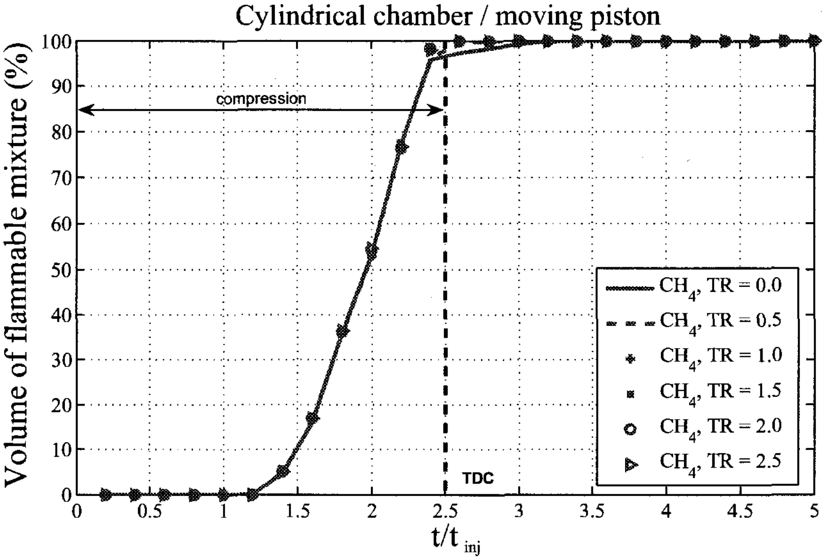

Fig. 4.21: Volume of flammable mixture vs. time at different tumble ratios in cylindrical chamber with moving piston; $U_{inj} = 300m/s$, $t_{inj} = 5ms$, $t_{sinj} = 6.25ms$.

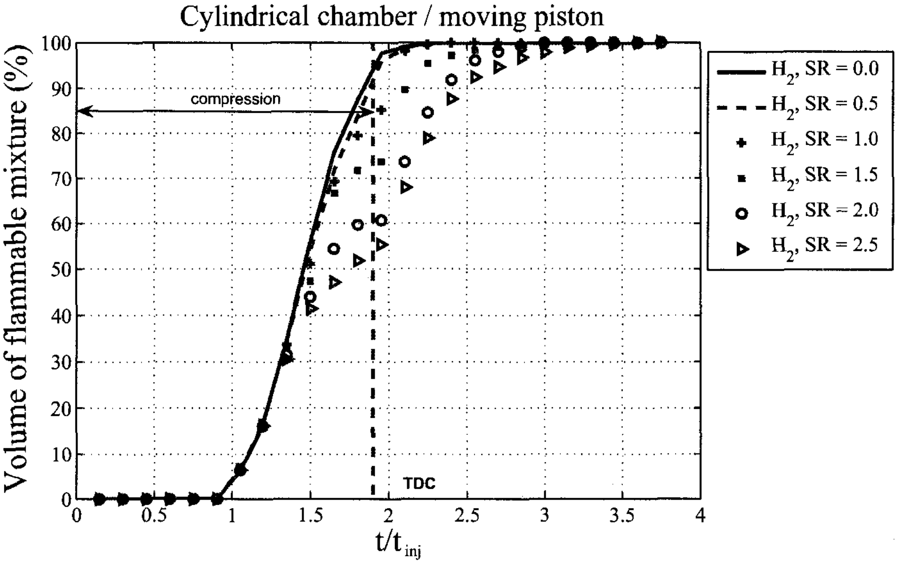

Fig. 4.22: Volume of flammable mixture vs. time at different swirl ratios in cylindrical chamber with moving piston; $U_{inj} = 450m/s$, $t_{inj} = 6.6ms$, $t_{sinj} = 6.25ms$.

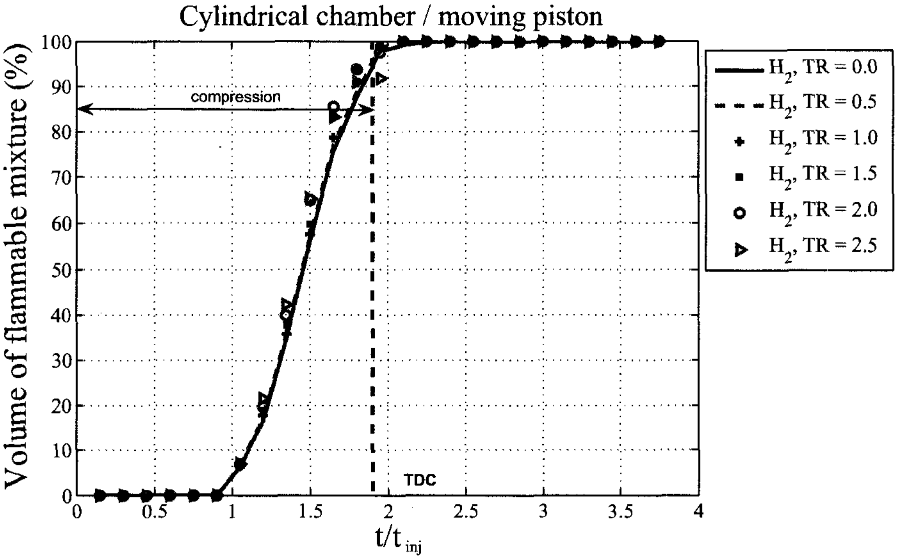

Fig. 4.23: Volume of flammable mixture vs. time at different tumble ratios in cylindrical chamber with moving piston; $U_{inj} = 450m/s$, $t_{inj} = 6.6ms$, $t_{sinj} = 6.25ms$.

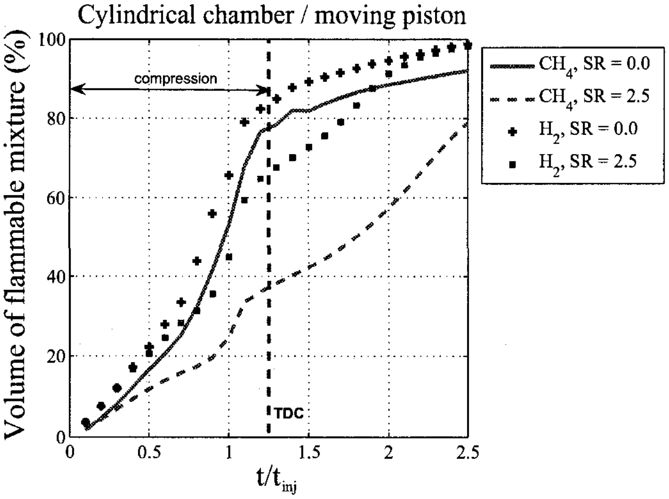

Fig. 4.24: Comparison of flammable mixture formation between H_2 and CH_4 at two different swirl ratios in cylindrical chamber with moving piston; CH_4: $U_{inj} = 150m/s$, $t_{inj} = 10ms$, $t_{sinj} = 0$; H_2: $U_{inj} = 300m/s$, $t_{inj} = 10ms$, $t_{sinj} = 0$.

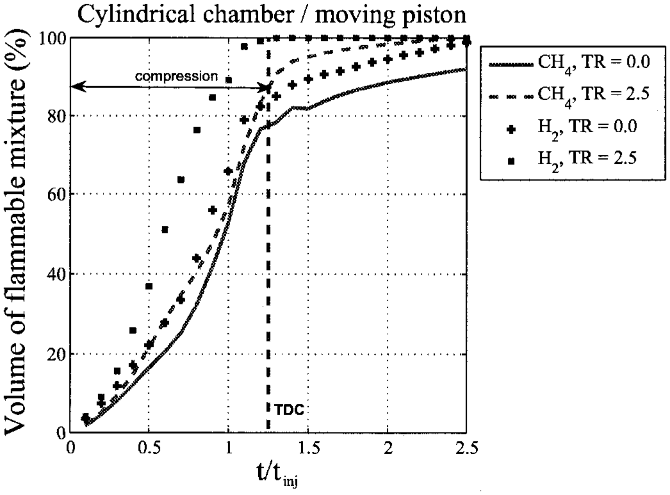

Fig. 4.25: Comparison of flammable mixture formation between H_2 and CH_4 at two different tumble ratios in cylindrical chamber with moving piston; CH_4: $U_{inj} = 150m/s$, $t_{inj} = 10ms$, $t_{sinj} = 0$; H_2: $U_{inj} = 300m/s$, $t_{inj} = 10ms$, $t_{sinj} = 0$.

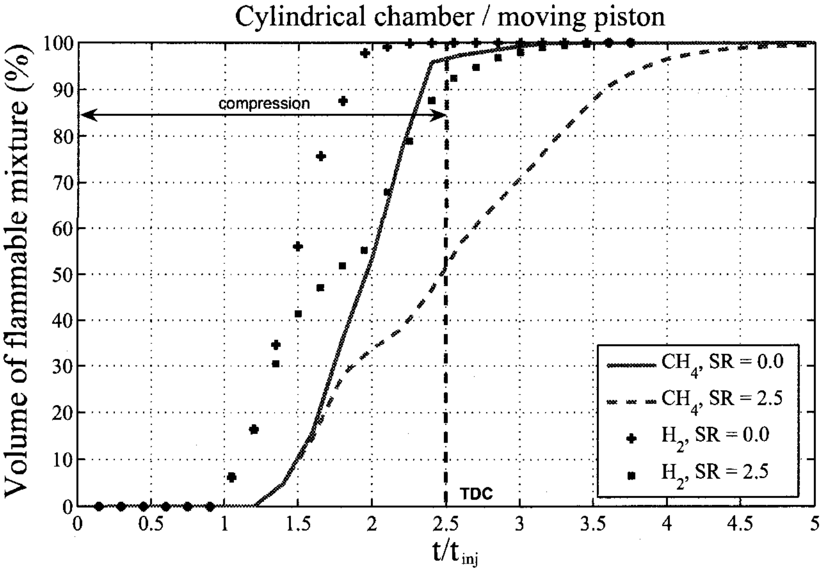

Fig. 4.26: Comparison of flammable mixture formation between H_2 and CH_4 at two different swirl ratios in cylindrical chamber with moving piston; CH_4:$U_{inj} = 300m/s$, $t_{inj} = 5ms$, $t_{sinj} = 6.25ms$; H_2: $U_{inj} = 450m/s$, $t_{inj} = 6.6ms$, $t_{sinj} = 6.25ms$.

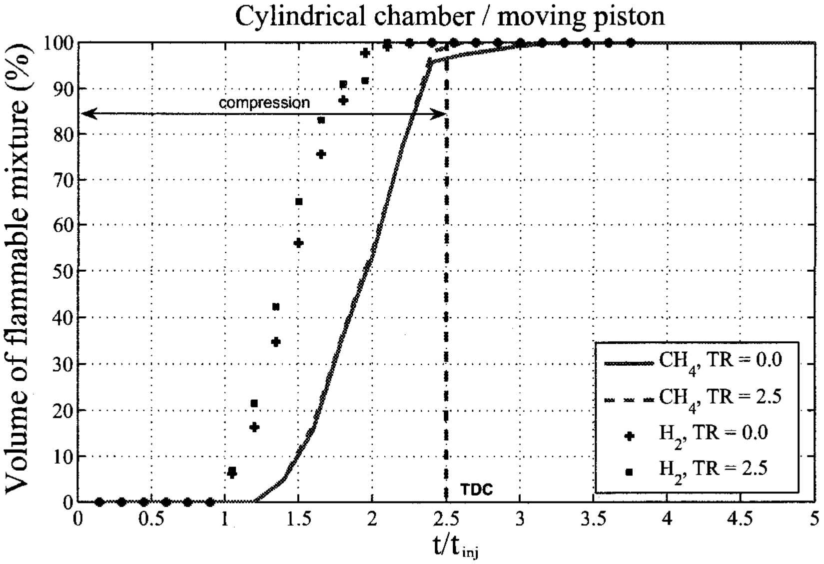

Fig. 4.27: Comparison of flammable mixture formation between H_2 and CH_4 at two different tumble ratios in cylindrical chamber with moving piston; CH_4: $U_{inj} = 300m/s$, $t_{inj} = 5ms$, $t_{sinj} = 6.25ms$; H_2: $U_{inj} = 450m/s$, $t_{inj} = 6.6ms$, $t_{sinj} = 6.25ms$.

4.3 Mixing Rate vs. time

Mixing rate at lowest and highest level of angular momentum for injection of methane and hydrogen are shown in Figures 4.28 to 4.31 in fixed volumes , cubic and cylindrical chambers. The mixture rate is higher where the air inside the chamber has a tumbling motion. It is also clear form the figures that the mixing rate has its high value during the injection period. The mixing rates for hydrogen are more sensible to the injection and and duration while mixing rate curves for methane slightly go up and then keep almost constant during mixing.

Mixing rates vs. time in cylinder with moving piston for maximum and minimum level of magnitude of bulk motion of air are shown in Figures 4.32 and 4.33 when the gaseous jet was injected at $t = 0$, and Figures 4.34 and 4.35 when injection time was set at $t = 6.25\,ms$. The rate of mixing is much closer compared to the fixed chambers considering hydrogen and methane as the injected fuel jet. Higher mixing rates are achieved when injection begins after half of the compression.

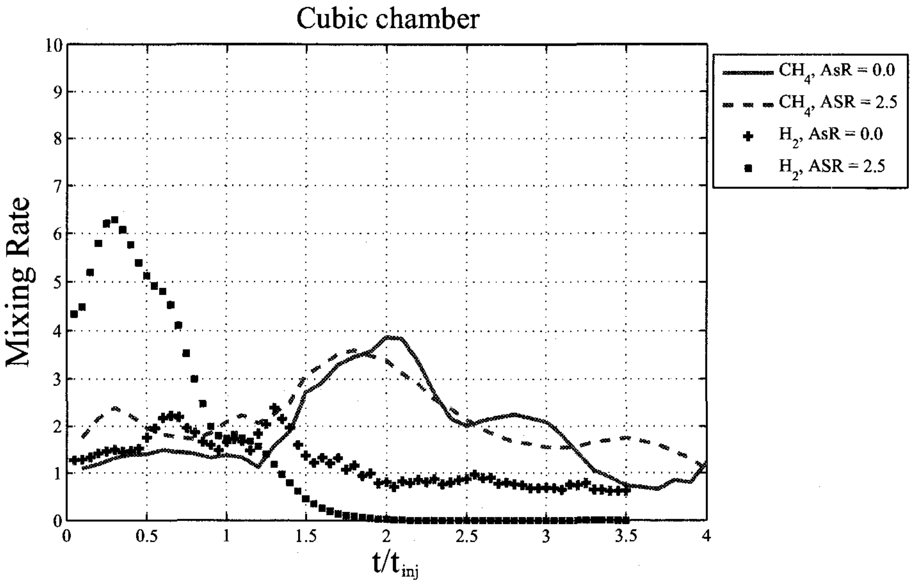

Fig. 4.28: Mixing rate vs. time at different swirl ratios in constant cubic volume chamber; CH_4: $U_{inj} = 150\,m/s$, $t_{inj} = 10\,ms$, $t_{sinj} = 0$; H_2: $U_{inj} = 150\,m/s$, $t_{inj} = 20\,ms$, $t_{sinj} = 0$.

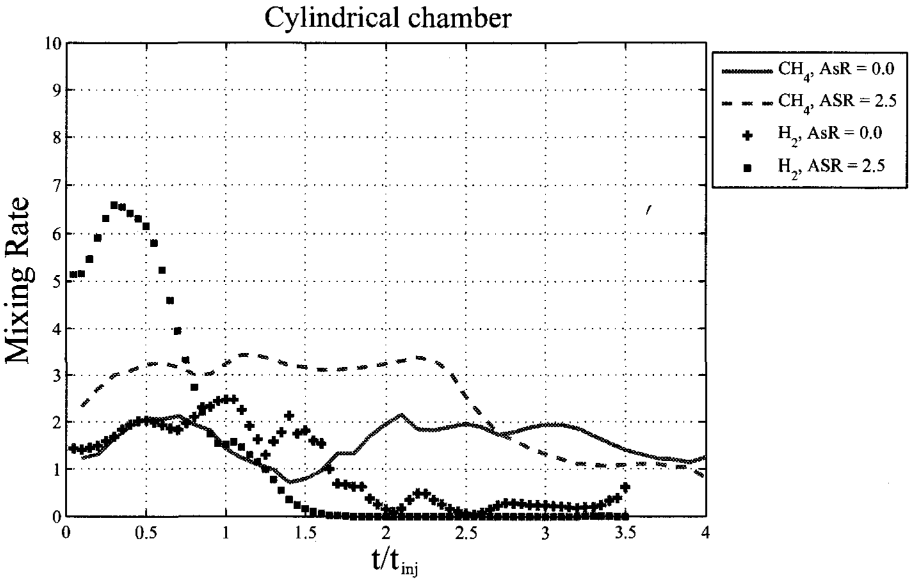

Fig. 4.29: Mixing rate vs. time at different swirl ratios in constant cylindrical volume chamber; CH_4: $U_{inj} = 150\,m/s$, $t_{inj} = 10\,ms$, $t_{sinj} = 0$; H_2: $U_{inj} = 150\,m/s$, $t_{inj} = 20\,ms$, $t_{sinj} = 0$.

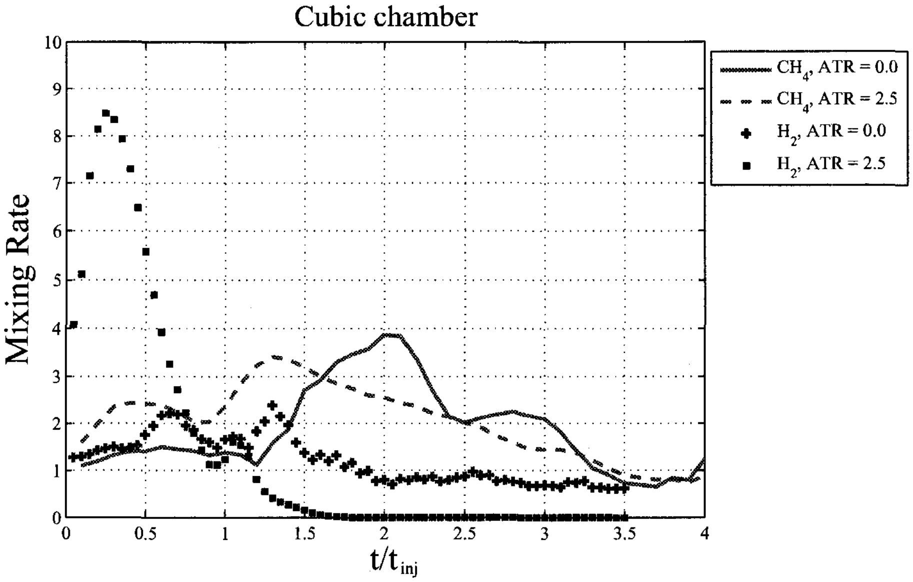

Fig. 4.30: Mixing rate vs. time at different tumble ratios in constant cubic volume chamber; CH_4: $U_{inj} = 150\,m/s$, $t_{inj} = 10\,ms$, $t_{sinj} = 0$; H_2: $U_{inj} = 150\,m/s$, $t_{inj} = 20\,ms$, $t_{sinj} = 0$.

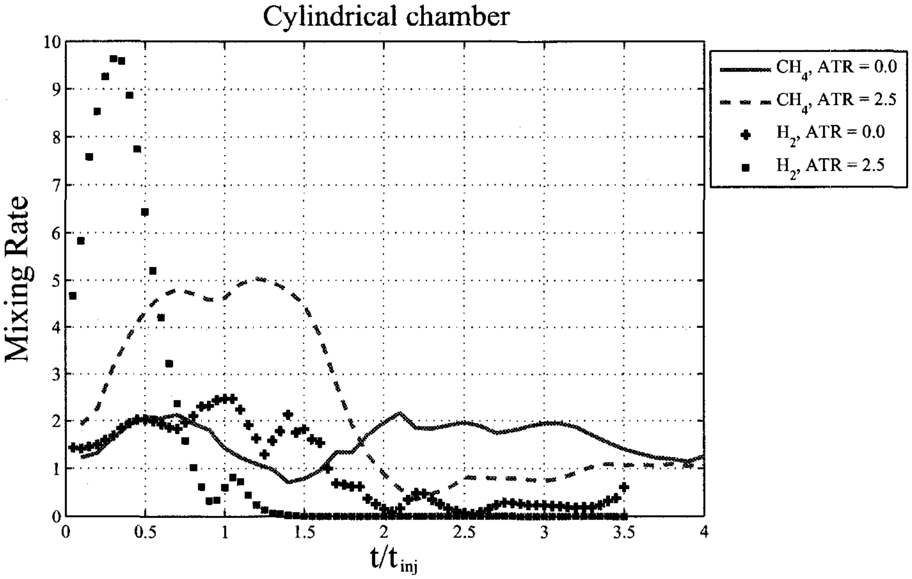

Fig. 4.31: Mixing rate vs. time at different tumble ratios in constant cylindrical volume chamber; CH_4:($U_{inj} = 150\,m/s$, $t_{inj} = 10\,ms$, $t_{sinj} = 0$; H_2: $U_{inj} = 150\,m/s$, $t_{inj} = 20\,ms$, $t_{sinj} = 0$.

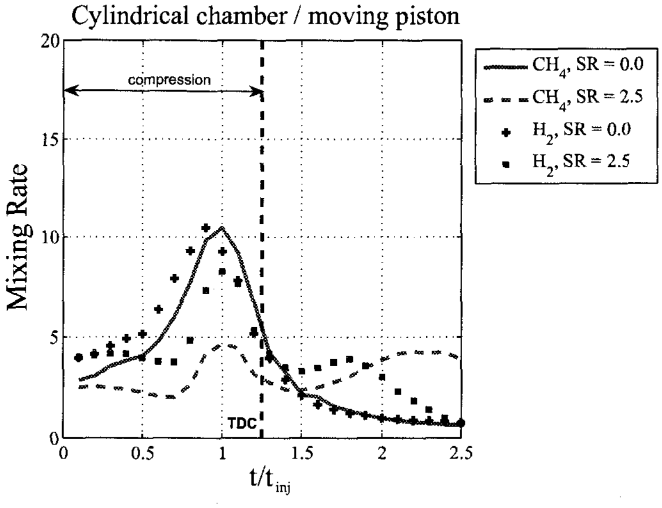

Fig. 4.32: Mixing rate vs. time at different swirl ratios in cylindrical chamber with moving piston; CH_4: $U_{inj} = 150m/s$, $t_{inj} = 10ms$, $t_{sinj} = 0$; H_2: $U_{inj} = 300m/s$, $t_{inj} = 10ms$, $t_{sinj} = 0$.

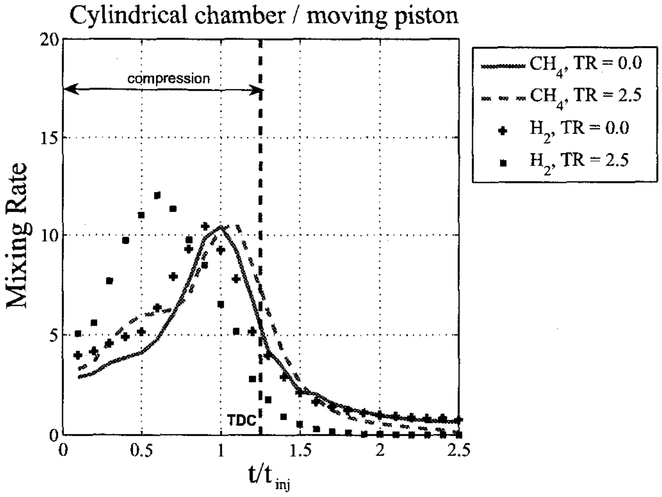

Fig. 4.33: Mixing rate vs. time at different swirl ratios in cylindrical chamber with moving piston; CH_4: $U_{inj} = 150m/s$, $t_{inj} = 10ms$, $t_{sinj} = 0$; H_2: $U_{inj} = 300m/s$, $t_{inj} = 10ms$, $t_{sinj} = 0$.

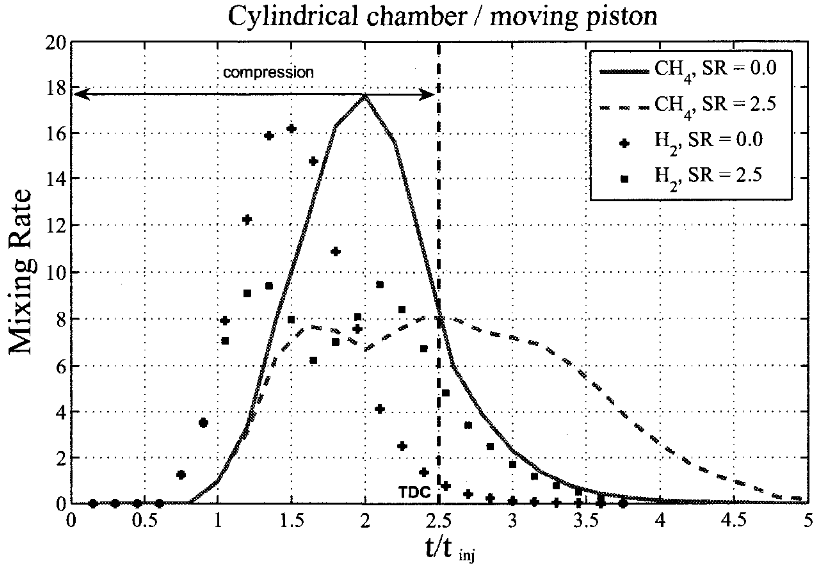

Fig. 4.34: Mixing rate vs. time at different swirl ratios in cylindrical chamber with moving piston; CH_4: $U_{inj} = 300m/s$, $t_{inj} = 5ms$, $t_{sinj} = 6.25ms$; H_2: $U_{inj} = 450m/s$, $t_{inj} = 6.6ms$, $t_{sinj} = 6.25ms$.

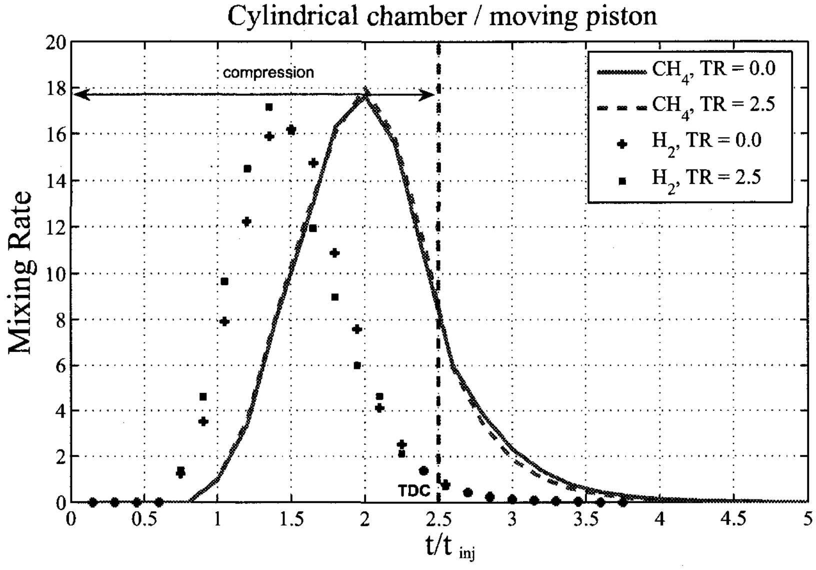

Fig. 4.35: Mixing rate vs. time at different swirl ratios in cylindrical chamber with moving piston; CH_4: $U_{inj} = 300m/s$, $t_{inj} = 5ms$, $t_{sinj} = 6.25ms$; H_2: $U_{inj} = 450m/s$, $t_{inj} = 6.6ms$, $t_{sinj} = 6.25ms$.

4.4 Angular Momentum Behavior

The behavior of angular momentum is shown in Figures 4.36 and 4.37. The calculation were done on a plane. Calculation of tumble were done on a plane cut through the injector and for swirl in a moving plane located in the center between cylinder head and piston. The results represent the angular momentum change at different swirl and tumble ratios in the cylindrical chamber with moving piston. It is clear that tumbling motion of air decays faster than swirling motion. While tumbling motion almost disappears during the expansion stroke, swirling motion shows an increase during compression and then it decreases when the piston goes from TDC to BDC.

It should be noted that the flammable charge of air and fuel in most of the engine applications is provided during the compression stroke, and ignited slightly after TDC. Ignition after TDC prevents negative work created by combustion pressure. Therefore, car manufacturing companies and researchers are becoming more interested in providing tumbling motion in the cylinder, because of its better effect in mixture formation.

Injection of gaseous fuel adds angular momentum to the bulk motion of air having tumbling rotation. The jet travels through the bulk motion and divides it into two vortices rotating on each side of the jet. Movement of the piston toward TDC makes them disappear. There is no bulk motion of air in the expansion stroke.

When swirling motion is available in the cylinder, injection of gaseous fuel does not have as much effect as the movement of the piston. Conservation of angular momentum makes it rotates faster but, since its axis is the same as the injector nozzle, it can not enhance mixing as expected.

The angular momentum integrated in total volume are shown in Figures 4.40 to 4.43. The effect of injection on the swirling and tumbling motion are also shown in Figure 4.44 and Figure 4.45. The results show the huge influence of bulk motion by the injection process. The injection becomes more important when it comes to the tumbling motion.

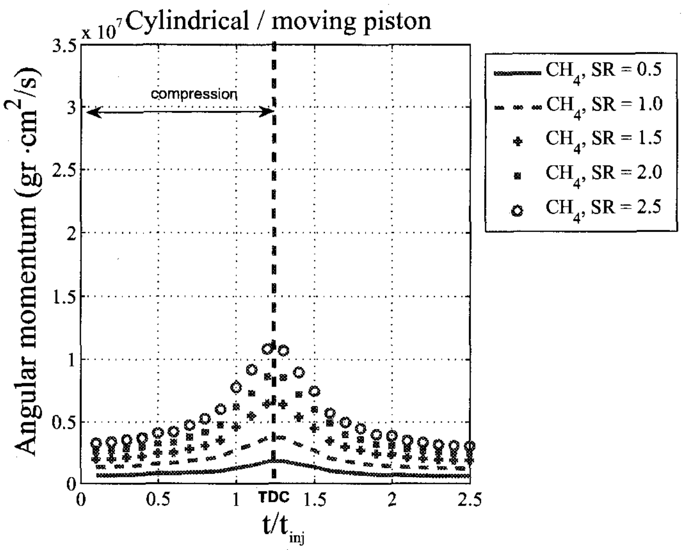

Fig. 4.36: Angular momentum change time at different swirl ratios in cylindrical chamber with moving piston; $U_{inj} = 150m/s$, $t_{inj} = 10ms$, $t_{sinj} = 0$, calculated at the moving plane half way between the piston and engine head.

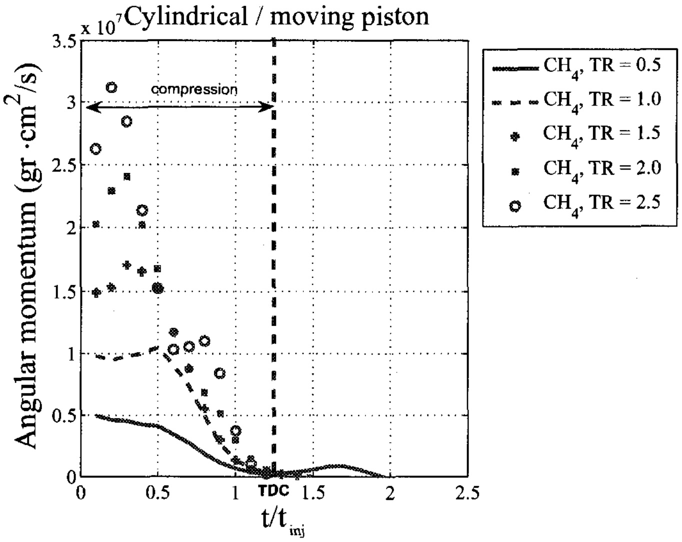

Fig. 4.37: Angular momentum change time at different tumble ratios in cylindrical chamber with moving piston; $U_{inj} = 150m/s$, $t_{inj} = 10ms$, $t_{sinj} = 0$, calculated at centerline plane.

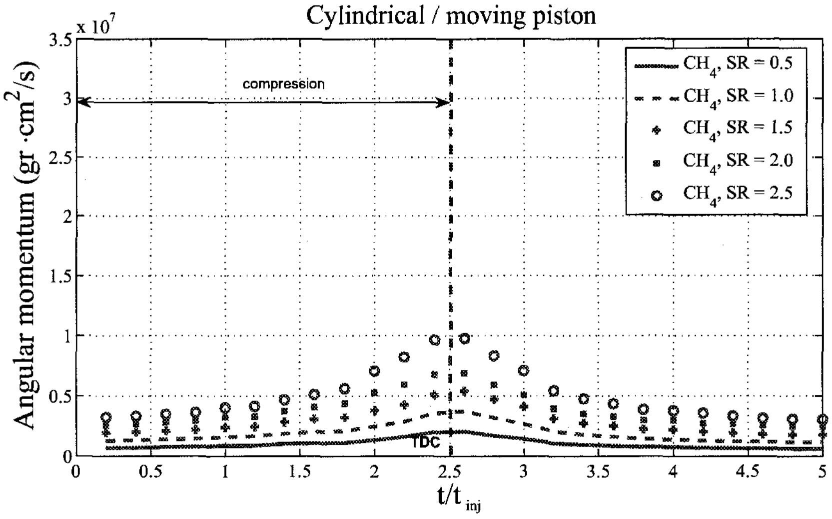

Fig. 4.38: Angular momentum change time at different swirl ratios in cylindrical chamber with moving piston. $U_{inj} = 300m/s$, $t_{inj} = 5ms$, $t_{sinj} = 6.25ms$, calculated at the moving plane half way between the piston and engine head.

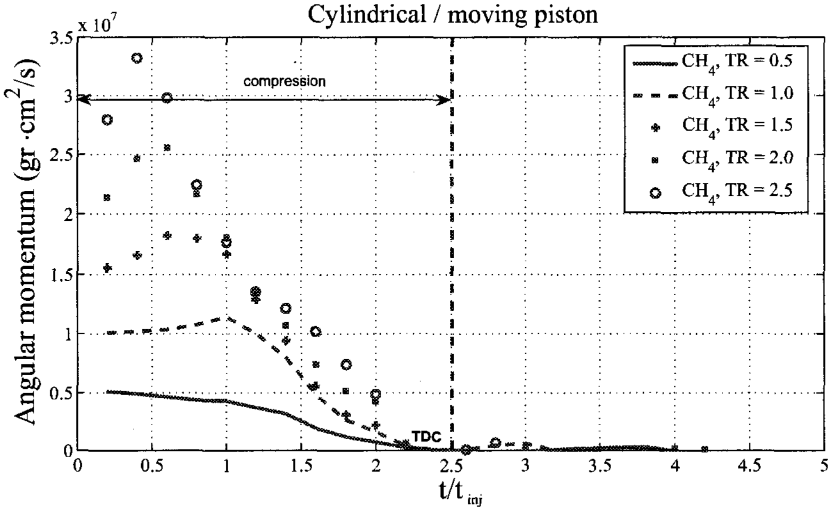

Fig. 4.39: Angular momentum change time at different tumble ratios in cylindrical chamber with moving piston. $U_{inj} = 300m/s$, $t_{inj} = 5ms$, $t_{sinj} = 6.25ms$, calculated at centerline plane.

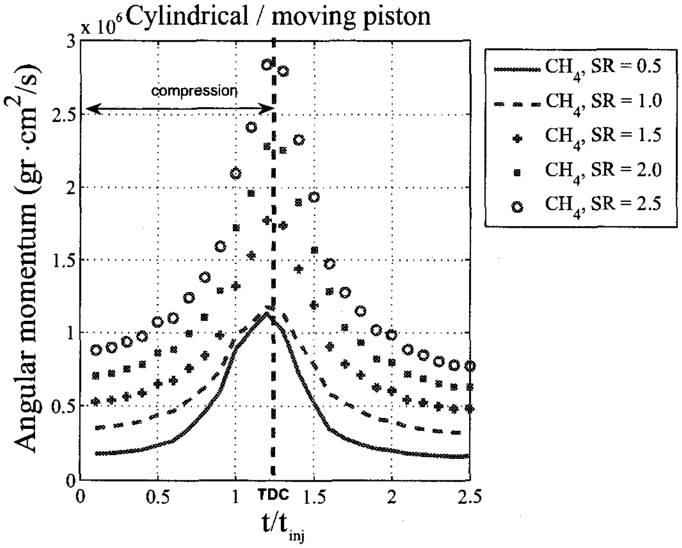

Fig. 4.40: Angular momentum change time at different swirl ratios in cylindrical chamber with moving piston; $U_{inj} = 150 m/s$, $t_{inj} = 10 ms$, $t_{sinj} = 0$, calculated for the entire volume above the moving piston.

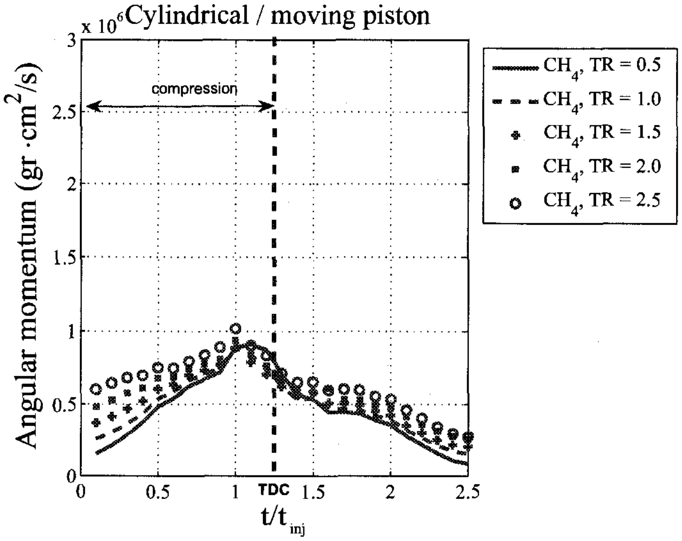

Fig. 4.41: Angular momentum change time at different tumble ratios in cylindrical chamber with moving piston; $U_{inj} = 150 m/s$, $t_{inj} = 10 ms$, $t_{sinj} = 0$, calculated for the entire volume above the moving piston.

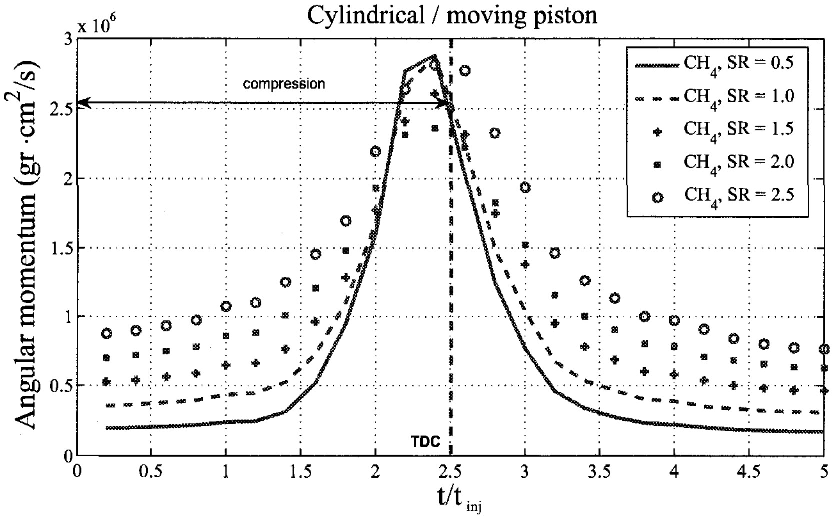

Fig. 4.42: Angular momentum change time at different swirl ratios in cylindrical chamber with moving piston. $U_{inj} = 300m/s$, $t_{inj} = 5ms$, $t_{sinj} = 6.25ms$, calculated for the entire volume above the moving piston.

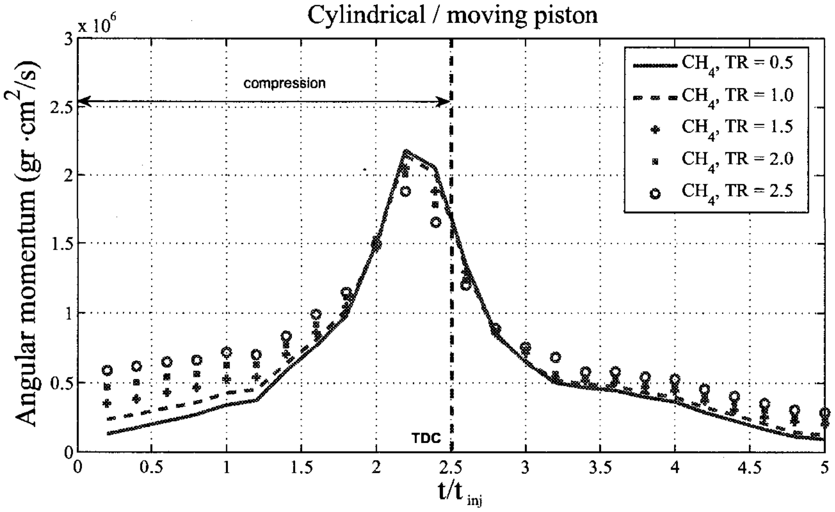

Fig. 4.43: Angular momentum change time at different tumble ratios in cylindrical chamber with moving piston. $U_{inj} = 300m/s$, $t_{inj} = 5ms$, $t_{sinj} = 6.25ms$, calculated for the entire volume above the moving piston.

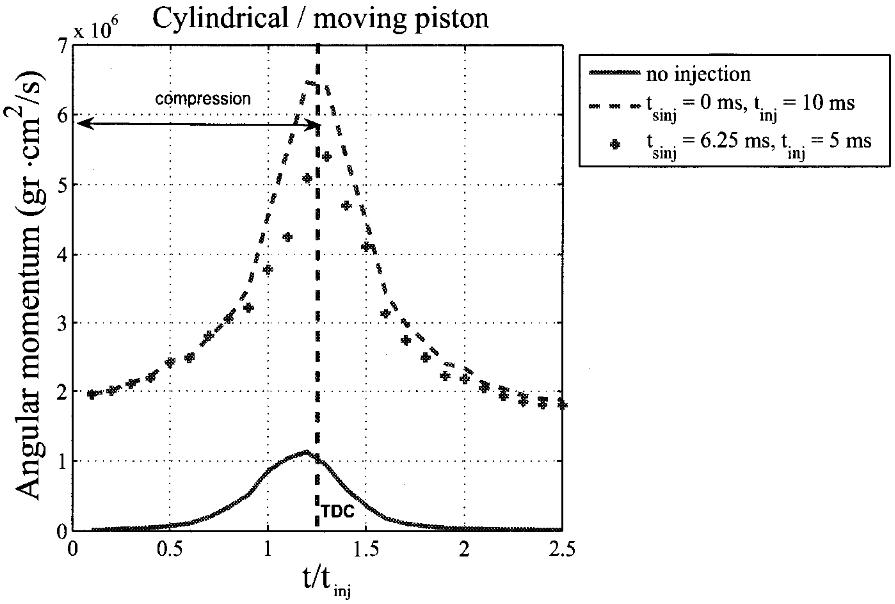

Fig. 4.44: Angular momentum change time at different injection time for CH_4, SR = 3, time was normalized by $t_{inj} = 10\, ms$.

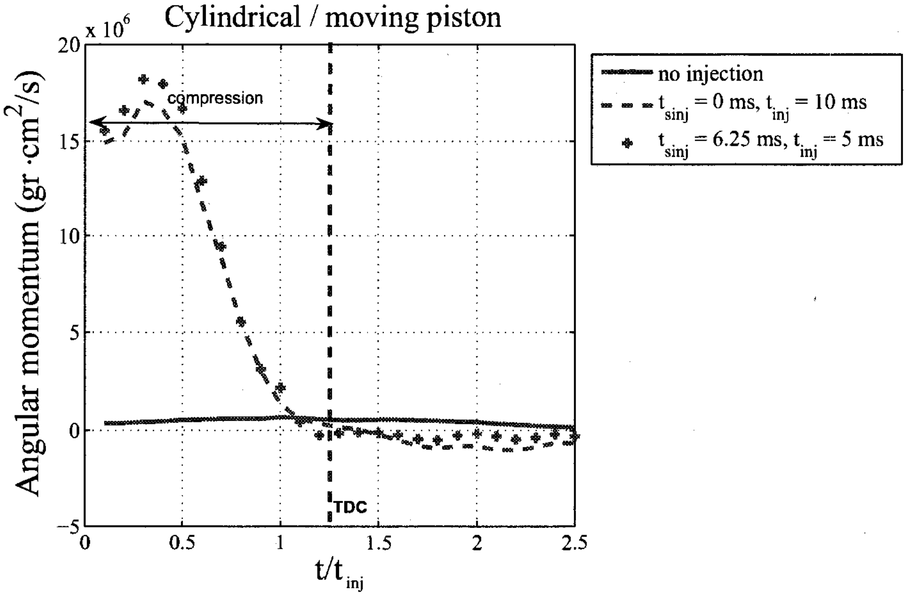

Fig. 4.45: Angular momentum change time at different injection time for CH_4, TR = 3, time was normalized by $t_{inj} = 10\, ms$.

Chapter 5

Conclusions and Recommendations

5.1 Conclusions

In this study the effects of angular momentum (tumble and swirl) on flammable mixture formation between chamber air and transient gaseous jets of hydrogen and methane were numerically investigated in fixed volumes, cubic and cylindrical chambers, and in a variable volume cylindrical chamber with moving piston. The magnitude of the angular momentum, injection duration, and injection velocity are the main parameters whose effects were studied on flammable mixture formation and mixing rate. The numerical simulations were carried out with the use of KIVA3V. The code is modified for gaseous injection with standard $k-\epsilon$ model for turbulence.

The geometries employed in this work were created with K3PREP, the mesh generation package available in KIVA3V. The fixed volume chambers are selected so that they have the same total volume. The variable volume chamber is identical to the fixed cylindrical chamber when the piston is located at BDC. The crankshaft rotates with *rpm* of 2400 and the compression ratio is 10. Mesh sensitivity analysis has also been carried out.

- The results show that employing a finer mesh not significantly change the volume of flammable mixture.

- Increasing tumble or swirl ratio leads to better mixture formation in fixed volumes, while in the cylindrical chamber with moving piston there is an optimum value for the ratio of angular momentum of air to that of engine *rpm*. Furthermore, it was found that tumbling motion of air serves better than swirl motion in mixture preparation in all the cases under study.

- The impact of type of the geometry was studied by injecting gaseous fuel into two fixed volume, cubic and cylindrical chambers. Better mixing is obtained in the cylindrical chamber.

- The evolution of angular momentum of swirling and tumbling motion in the cylindrical chamber with moving piston, was numerically modeled. The results show the following:

  1) An increase of angular momentum for both swirling and tumbling motion is due to fuel injection.

  2) The angular momentum decays when piston moving up for tumbling motion, and it amplified for swirling motion when piston moving up.

5.2 Recommendations

Based on the current work, the following recommendations are suggested;

1. Relocating center of tumble and swirl. Having center of tumbling or swirling motion of air at some point other than center of the cube or cylinder can change the symmetry and perhaps have different effects on mixing formation.

2. Using combination of swirl and tumble. This can model the impact of valve shapes and piston head geometry in real engines.

3. Changing turbulent kinetic energy and length scale. High level of turbulent kinetic energy inside the chamber can increase the entrainment rate and subsequently affect

the volume of flammable mixture.

4. Angled injection. Injection with the same direction of tumbling motion or against it would change the angular momentum and mixing process. With swirling motion, the jet can be injected off the center of the swirling motion and lead to a different trend in mixing.

5. Vary mass of injection to create different overall equivalence ratio. Start of injection, injection duration and injection velocity are the parameters controlling total equivalence ration in the cylinder. Different values can be used for different applications.

6. Employing different turbulence sub-models.As $k-\epsilon$ model cannot model anisotropy in the Reynolds stress tensor, using a different turbulence model may result in better prediction of mixture formation inside the chambers.

7. Comparing with experiment. For this work, no experimental results were found to compare with the results of simulation. Designing some experiment in future would help to verify the results.

Appendix A

Governing Equations

The equations of motion of fluid phase and boundary conditions employed in KIVA3V are given in this appendix. For compactness, these are written in vector notation with bold symbols representing vector and tensor quantities. The unit vectors in x, y, and z directions are denoted by $\mathbf{i}$, $\mathbf{j}$, $\mathbf{k}$ respectively. The position vector $\mathbf{x}$ is defined by

$$\mathbf{x} = x\mathbf{i} + y\mathbf{j} + z\mathbf{k} \tag{A.1}$$

the vector operator ∇ is given by

$$\nabla = \mathbf{i}\frac{\partial}{\partial x} + \mathbf{j}\frac{\partial}{\partial y} + \mathbf{k}\frac{\partial}{\partial z} \tag{A.2}$$

and the fluid velocity vector $\mathbf{u}$ is given by,

$$\mathbf{u} = u(x, y, z, t)\mathbf{i} + v(x, y, z, t)\mathbf{j} + w(x, y, z, t)\mathbf{k} \tag{A.3}$$

where t is time.

KIVA3V equations can be used to solve for both laminar and turbulent flows. The mass, momentum, and energy equations for the two cases differ primarily in the form and magnitude of the transport coefficients (i.e., viscosity, thermal conductivity, and species diffusivity), which are much larger in the turbulence case because of the additional transport caused by turbulent fluctuations. In the turbulent case the transport coefficients are derived from a turbulent diffusivity that depends on the turbulent kinetic energy and its dissipation rate.

The continuity equation for species m is

$$\frac{\partial \rho_m}{\partial t} + \nabla \cdot (\rho_m \mathbf{u}) = \nabla \cdot [\rho D \nabla (\frac{\rho_m}{\rho})] \tag{A.4}$$

where ρ_m is the mass density of species m, ρ is the total mass density, and $\mathbf{u}$ is the fluid velocity. Fick's law is assumed with the single coefficient D. By summing Eq. (A.4) over all species, the total fluid density equation is obtained,

$$\frac{\partial \rho}{\partial t} + \nabla \cdot (\rho \mathbf{u}) = 0. \tag{A.5}$$

The momentum equation for the fluid mixture is

$$\frac{\partial (\rho \mathbf{u})}{\partial t} + \nabla \cdot (\rho \mathbf{u}\mathbf{u}) = -\nabla p - A_0 \nabla (2/3 \rho k) + \nabla \cdot \sigma + \rho \mathbf{g} \tag{A.6}$$

where p is the fluid pressure, k is the turbulent kinetic energy, and $\mathbf{g}$ is the gravity vector. The quantity A_0 is set to zero in laminar flow calculation and to unity when a turbulence model is used. The viscous tensor is Newtonian in form:

$$\sigma = \mu[\nabla \mathbf{u} + (\nabla \mathbf{u}^T)] + \lambda \nabla \cdot \mathbf{u}\mathbf{I} \tag{A.7}$$

where μ and λ are coefficients of viscosity. The superscript T denotes the transpose and $\mathbf{I}$ is the unit dyadic.

The internal energy equation is

$$\frac{\partial(\rho I)}{\partial t} + \nabla \cdot (\rho \mathbf{u} I) = -p\nabla \cdot \mathbf{u} + (1 - A_0)\sigma : \nabla \mathbf{u} - \nabla \cdot \mathbf{J} + A_0 \rho \epsilon \tag{A.8}$$

where I is the specific internal energy. The heat flux vector $\mathbf{J}$ is the sum of contributions due to heat conduction and enthalpy diffusion,

$$\mathbf{J} = -K\nabla T - \rho D \sum_m h_m \nabla(\rho_m/\rho) \tag{A.9}$$

where T is the fluid temperature and h_m is the specific enthalpy of species m.

Transport equations for turbulent kinetic energy k and dissipation rate ϵ are,

$$\frac{\partial(\rho k)}{\partial t} + \nabla \cdot (\rho \mathbf{u} k) = -\frac{2}{3}\rho k \nabla \cdot \mathbf{u} + \sigma : \nabla \mathbf{u} + \nabla \cdot [(\frac{\mu}{Pr_k})\nabla k] - \rho\epsilon \tag{A.10}$$

and

$$\frac{\partial(\rho \epsilon)}{\partial t} + \nabla \cdot (\rho \mathbf{u} \epsilon) = -(\frac{2}{3}c_{\epsilon_1} - c_{\epsilon_3})\rho\epsilon \nabla \cdot \mathbf{u} + \nabla \cdot [(\frac{\mu}{Pr_\epsilon})\nabla \epsilon] + \frac{\epsilon}{k}[c_{\epsilon_1}\sigma : \nabla \mathbf{u} - c_{\epsilon_2}\rho\epsilon] \tag{A.11}$$

The source term $(\frac{2}{3}c_{\epsilon_1} - c_{\epsilon_3})\nabla \cdot \mathbf{u}$ in Eq. (A.11) accounts for length scale changes when there is velocity dilatation. The quantities c_{ϵ_1}, c_{ϵ_2}, c_{ϵ_3}, Pr_k, and Pr_ϵ are constants whose values are determined from experiments and some theoretical considerations. Standard values of these constants used in this study are:

$c_{\epsilon_1} = 1.44$, $c_{\epsilon_2} = 1.92$, $c_{\epsilon_3} = -1.0$, $Pr_k = 1.0$, and $Pr_\epsilon = 1.3$.

The state relations are assumed to be those of an ideal gas mixture. Therefore,

$$p = R_0 T \sum_m (\rho_m / W_m) \tag{A.12}$$

$$I(T) = \sum_m (\rho_m/\rho) I_m(T) \tag{A.13}$$

$$c_p(T) = \sum_m (\rho_m/\rho) c_{pm}(T) \tag{A.14}$$

and

$$h_m(T) = I_m(T) + R_0 T/W_m \tag{A.15}$$

where R_0 is the universal gas constant, W_m is the molecular weight of species m, and $I_m(T)$ is the specific internal energy of species m.

References

[1] P. Ouellette. *Direct Injection of Natural Gas for Diesel Engine Fueling.* PhD dissertation, University of British Columbia, 1996.

[2] C. Xia. *The behaviour of agaseous transient jet in a direct injection turbulence chamber.* PhD dissertation, University of Windsor, 2006.

[3] G. K. Bachelor. *An introduction to Fluid Dynamics.* Cambridge press, 1967.

[4] M. Van Dyke. *An album of Fluid Motion.* Parabolic Press, 1988.

[5] A. Chepakovich. Visualization of transient single and two phase jets created by diesel engine injectors. Master's thesis, University of British Columbia, 1993.

[6] G. N. Abramovich. *The Theory of Turbulent Jets.* MIT Press, 1963.

[7] E. Tomita, Y. Hamamoto, S. Yoshiyama, H. Tsutsumi, and T. Watanabe. Ambient air entrainment into transient hydrogen jet and its flame jet. Technical Report 970894, SAE Technical Paper Series, 1997.

[8] T. Alger, M. Hall, and R. D. Matthews. Effects of swirl and tumble on in-cylinder fuel distribution in a central injected DISI engine. Technical Report 2000-01-0533, SAE Technical Paper Series, 2000.

[9] H. Baumgarten, P. Bozelie, J. Geiger, and P. Wolters. Vehicle application of a 4-cylinder tumble DISI engine. Technical Report 2001-01-0735, SAE Technical Paper Series, 2001.

[10] A. Devesa, J. Moreau, T. Poinsot, and J. Helie. Large eddy simulations of jet / tumble interaction in a GDI model engine flow. Technical Report 2004-01-1997, SAE Technical Paper Series, 2004.

[11] A. Floch, J. Van Frank, and A. Ahmed. Comparison of the effects of intake-generated swirl and tumble on turbulence characteristics in a 4-valve engine. Technical Report 952457, SAE Technical Paper Series, 1995.

[12] P. G. Hill and P. Ouellette. Transient turbulent gaseous fuel jets for diesel engines. *ASME J. Fluids Eng.*, 121:93–101, 1999.

[13] L. Shuliang, L. Yufeng, and L. Ming. Prediction of tumble speed in the cylinder of the 4-valve spark ignition engines. Technical Report 2000-01-0247, SAE Technical Paper Series, 2000.

[14] Y. Li, H. Zhao, and N. Ladommatos Z. Peng. Analysis of tumble and swirl motions in a four-valve Si engine. Technical Report 2001-01-3555, SAE Technical Paper Series, 2001.

[15] T. Tsujimura, S. Mikami, N. Achiha, Y. Tokunaga, J. Senda, and H. Fujimoto. A study of direct injection diesel engine fueled with hydrogen. Technical Report 2003-01-0761, SAE Technical Paper Series, 2003.

[16] K. Koyanagi, M. Hiruma, K. Yamane, and S. Furuhama. Effect of hyrogen jet on mixture formation in high-pressure injection hydrogen fueled engine with spark ignition. Technical Report 931811, SAE Technical Paper Series, 1993.

[17] S. Kaiser and C.M. White. PIV and PLIF to evaluae mixture formation in a direct-injection hydrogen-fuelled engine. Technical Report 2008-01-1034, SAE Technical Paper Series, 2008.

[18] P. Stansfield, G. Wigley, T. Justham, J. Catto, and G. Pitcher. PIV analysis of in-cylinder flow structures over a range of realistic engine speed. *Experiments in Fluids*, 146:43–135, 2007.

[19] C. W. Hong and S. D. Trang. In cylinder tumble flow field measurments and predictions. *Journal of Engineering for Gas Turbine and Power*, 123:139–145, 2001.

[20] A. A. Amsden, P. J. O' Rourke, and T. D. Butler. KIVA-II a computer program for chemically reactive flows with sprays. Technical Report LA-11560-MS, LANL, 1989.

[21] A. A. Amsden. KIVA-3V a block-structured kiva program for engines with vertical or canted valves. Technical Report LA-13313-MS, LANL, 1997.

[22] S. Wahiduzzaman and C.R. Ferguson. Convective heat transfer from a decaying swirling flow within a cylinder. In *8th International heat transfer conference*, number 86-IHTC-253, 1986.

[23] J. Abraham. What is adequate resolution in numerical compuatations of transient jets. Technical Report 970051, SAE Technical Paper Series, 1997.